Broadband Study of Cassiopeia A

Breitbandstudie von Cassiopeia A

Fabian Moritz Boeck

03617787

Abschlussarbeit im Bachelorstudiengang Physik

Physik-Department
Technische Universität München

Erstgutachter:	Prof. Dr. Roland Diehl
Zweitgutachter:	Hubert Kroha
Abgabedatum:	20. Oktober 2016

Max Planck Institute for extraterrestrial physics
Department of high energy astronomy

Abstract. In essence, this thesis serves as an introduction to stellar astronomy and a compilation of analytical methods to assess the properties of stellar objects, in particular the expanding debris in the aftermath of a star's explosion at the example of the supernova remnant Cassiopeia A. Throughout the text, the presentation is directed at readers with little precognition of astronomy and aimed at providing an inherently consistent foundation for further acquisition of more specific knowledge. In this spirit, clear and modest illustrations are preferred to overly meticulous attention to detail in order to convey an adequately broad coverage in a conclusive manner, condoning the resulting appearance of superficiality.

As an introduction to the variety of stellar astronomy, the evolutionary stages of a star and the underlying processes are discussed, starting at the fragmentation of molecular clouds, the outlines of a star's nativity conditions and its subsequent paths on the Hertzsprung-Russel diagram while highlighting the correlations between properties and observables. To expand the previously structure-oriented reviewed stellar evolution process and to accentuate the concept of a star and a supernova remnant as a shell-like structure, stellar nucleogenesis mechanisms, their occurence and their eventual reflection in the remnant's composition are presented.

The plurality of supernova mechanisms and the presumed attribution to the spectral classification are displayed in concise manner, followed by an overview over the remnant's evolutionary stages, largely dropping the topic of the star's compact remainder. Concluding the theoretical part, detailed explanations about the respective observables in the remnant's spectrum, their origins and limitations and analytical treatment and their individual contributions to a substantial insight into a stellar object are introduced.

Moving over to Cassiopeia A, the analysis starts by depicting the investigation of the most basic properties step by step by applying the techniques described in the previous part in discerning manner, in particular the age by proper motion measurement, distance by spherically fitting Doppler shifts and location and kinematics of the forward and reverse shock analogously. Comparison with an evolutionary model demonstrates that the remnant is in the Sedov-phase. The presumed identity of the remaining compact object as an anti-magnetar is mentioned briefly for the sake of completion without throughout discussion as an adequate dissection go beyond the scope of this thesis. Delving further in the geometric properties, the different asymmetries as the piston and tilted disk structure in the shocked plateau and the dense filaments in the unshocked ejecta are discussed and related to asymmetric incongruities in the reverse shock expansion.

After the morphological features are compiled, traces of Cassiopeia A's past in form of light echoes are pursued, revealing the remnant to have emerged from a Type IIb supernova and that the asymmetries causing the piston-like structures formed shortly after the explosion. To show constraints on the ejecta and thereby getting a better picture of the remnant's progenitor, determination of the abundances of the tracer elements ^{44}Ti by direct observation and ^{56}Fe by elaborate investigation of the apparent subluminosity of the explosion on one hand and plasma modelling on the other is documented and reviewed in terms of validity; as a side product, estimates for explosion energy and progenitor are derived.

The presentation of Cas A is concluded by reevaluating the validity of the methods used in respect to the obtained results and theorizing a possible evolutionary history as well as the cause for the apparent subluminosity of the explosion.

Contents

List of Figures

List of Tables

List of Abbreviations

AGB	asymptotic giant branch
BH	black hole
BR	bright ring
Cas A	Cassiopeia A
CC	core collapse
COE	center of expansion
CR	cosmic ray
CSE	circumstellar envelope
CSM	circumstellar matter
E-AGB	early AGB
e.c.	electron capture
FHSC	first hydrostatic core
FMK	fast-moving knot
FS	forward shock
GMA	giant molecular association
GMC	giant molecular cloud
GRB	gamma ray burst
HRD	Hertzsprung-Russel-diagram
ISM	interstellar matter
LE	light echo
LOS	line of sight
MS	main sequence
NS	neutron star
PMS	pre main sequence
POS	plane of sky
RS	reverse shock
SASI	standing accretion shock instability
SN(e)	supernova(e)
SNR	supernova remnant
TAMS	terminal age main sequence
TP-AGB	thermally pulsing AGB
TR	thermal runaway
WD	white dwarf
ZAMS	zero age main sequence

1 Introduction

Supernovae (SNe) are complex processes where small perbutations can propagate significantly and alienate the expanding debris. Even if they were well-understood from a theoretical standpoint, their multitude of emergent properties turn large-scale models into rough approximations and sufficiently detailed simulations extremely demanding in required computational time. Because of this, direct observation of a supernova remnant's (SNR's) evolution is still the most effective way to research their diverse properties. While SNe can be observed frequently (about one per year), it is rare that a remnant is in such a proximity that its features can be spatially resolved in high detail.
Cassiopeia A (Cas A) is a comparably young ($\sim$ 336 yr) and nearby ($\sim$3.4 kpc) core collapse (CC-) SN. While its classification as the rare Type IIb already sets it apart from many other SNRs in the Milky Way, its morphology shows many irregular features, indicating large influence of atypical effects during the explosion. While the reasons for this are little more than speculations as of yet, the research of the remnant in the last two decades produced new and exciting insights about the geometry and history of Cas A at an ever growing pace.
There are still seemingly trivial questions unanswered about the remnant: For instance, the close SN should have been clearly visible on earth, however only one very faint sighting that appears to correspond to the collapse was passed down. Also, in only one other SN but Cas A were ^{44}Ti emissions directly observed; this is even becoming more puzzling as new models predict that this should be a rather common element in SNRs, albeit in smaller abundances, and implies that Cas A has indeed some very peculiar properties.
These irregular properties have caused multiple major errata that were accepted by significant parts of the research community in the past, most notably a presumed structure consisting of two semispheres of different radii, elemental shell inversions now known to actually be piston-like excrescences and near-inexplicably different speeds at the same location attributed to the very same shockwave, depending on the observed energy domain. While this is a natural property of the scientific process, it also serves as a warning that care must be taken when tackling the complex geometry.
This demands not only for lengthy consistency tests, but first and foremost a deep-routed understanding of the analytical process. In order to enable the reader to partake in mystery that is Cas A, this thesis starts with a basic introduction to the astronomy involved.

Part I
Theoretical Background

2 Stellar evolution

The evolution of stars is well-researched and widely ramified field. The models described herein are nothing more than an rough overview and describe the general tendencies; nearly every general statement comes with unmentioned exceptions.

2.1 Thermonuclear Phases of Stars

2.1.1 ISM Fragmentation

The matter between stars within a galaxy, the interstellar medium (ISM), often is highly turbulent and thereby inhomogeneous; high-density and low-energy regions can be compacted gravitationally. The most massive ($\approx 10^7 M_\odot$) resulting bound structures, so-called HI superclouds and giant molecular associations (GMAs), inherit high levels of turbulence; moreover, the spatially non-uniform compaction tends to amplify turbulences, inducing a second fragmentation

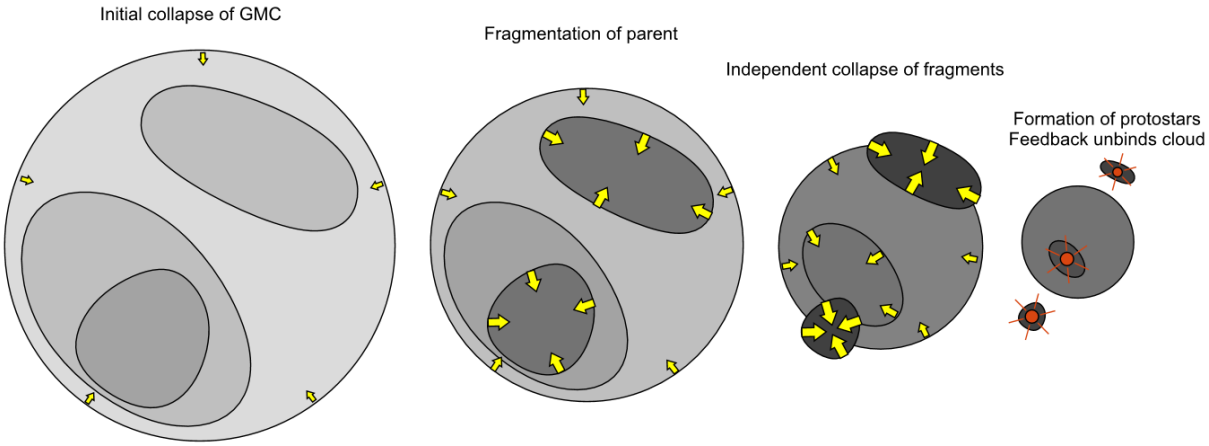

Figure 2.1: Simplified cartoon of the fragmentation during the turbulent gravitational collapse of GMCs (Source: Guszejnov and Hopkins 2016).

into giant molecular clouds (GMCs) (McKee and Ostriker 2007). The ISM's (and HI regions') composition is dominated by atomic hydrogen; supersonic turbulences in GMAs and GMCs lead to an interacting network of shock fronts, in whose high pressure regimes dust grains are used as catalyst (Gould and Salpeter 1963) to produce molecular hydrogen as well as traces of other molecules[1]. Eventually, the clouds consist of $\approx 70\%$ H_2 at average temperatures of 10-50 K.
In an analogous manner to the first two fragmentations, the GMCs collapse: First, the gravitational collapse of the cloud amplifies turbulences which steepens the density gradients and ultimately leads to self-gravitating clumps, so-called protostellar clouds[2]. These may initially be quasi-stable, meaning that there exists a density distribution in which gravity and pressure are in equilibrium, but as the gravitational accretion of surrounding gas increases the former and radiative cooling increases the latter, there is a critical point at which this equilibrium no longer exists. For an isothermal and spherical gas body of average particle mass μ in an ambient pressure p_0, this can be approximated by the Bonnor-Ebert-Relation[3]:

$$M_{BE} = \frac{C_{BE} k_B^2 T^2}{\mu^2 p_0^{1/2} G^{3/2}} \tag{2.1}$$

When this mass (typ. $10^3 - 10^4 M_\odot$) is surpassed, the protostellar clouds collapse individually and heat up in the process. Their increased blackbody radiation, among other effects, is believed to cushion the collapse of the GMC, stabilizing their position relative to the absolute center of gravity as shown in Figure 2.1. The increased density leads to a higher opacity, which makes radiative cooling, i.e. the energy loss caused by photoemissions, less efficient; when the temperature has reached about 60-100 K, the radiation pressure is sufficient to halt the collapse in the inner layers, a so-called first hydrostatic core (FHSC) with a typical radius of 10-20 AU[4] (Dunham et al. 2011) is created.

[1]Most notably, as the clouds are optically thick and H_2 shows no X-ray emissions in this temperature range, CO is used as a tracer to determine its abundance indirectly; studies produced an estimate ratio of $N[\mathrm{CO}]/N[\mathrm{H_2}] \approx (5 \pm 2.5) \times 10^{-5}$ (Dickman 1978).

[2]Protostellar clouds can also form in Bok globules, which are dense, opaque gas clouds which can form independently from GMCs (Khanzadyan et al. 2002)

[3]This can be derived from Equation 2.2 when inserting the ideal gas law the only pressure source. $C_{BE} \approx 1.18$ is the Bonnor-Ebert-constant, the other constants written with standard symbols. Another often-quoted approximation, the Jeans-criterium, which is based on a comparison of free falling time and speed of sound and assumes a homogeneous pressure in the cloud, showed less correlation in empirical tests.

[4]The astronomical unit is approximately the average distance between the earth and the Sun; 1AU$\approx 1.5 \times 10^{11}$m.

2.1.2 The Hertzsprung-Russel Diagram

A star is a near-ideal blackbody, meaning that the surface temperature unambiguously describes the output radiation output per surface area and time and relates to a peak in the radiation spectrum (see Chapter 4.1). When knowing its luminosity, i.e. the total radiation energy output of the star per time, the radius is given trivially; furthermore, only slightly blurred by the metallicity (see Chapter 2.1.7), the very regular behavior of most stars allows to deduce its mass. Thereby, it is practical to reduce a star to these two parameters as a first approximation so that stellar evolution can be displayed in a simple diagram, the so-called Hertzsprung-Russel diagram (HRD), where the very different processes in the respective phases lead to clearly distinguishable clusters as shown in figure 2.2 and will be elaborated in the following. Alternatively, the luminosity can be expressed in absolute magnitudes (see Chapter 4.2) and the surface temperature by a letter-based system based on the location of the peak as shown in the depicted HRD.

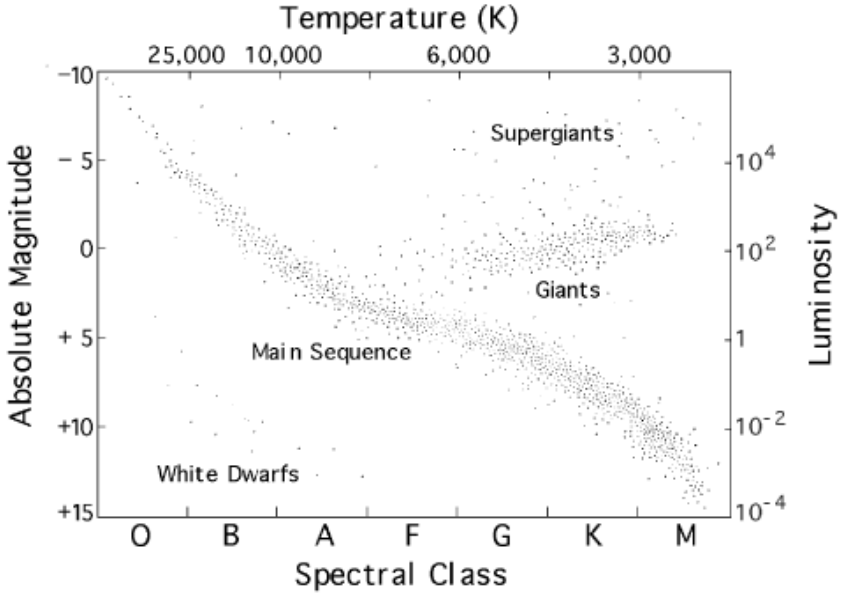

Figure 2.2: Star distribution on the HRD (Source: NASA)

2.1.3 Protostars

Infalling outer layers create shockwaves upon their collision with the FHSC, heating up the core to about 2000 K where H_2 may be dissociated again (Larson 1969) and ionisation of hydrogen and helium sets in. As the blackbody spectrum now reaches higher energies for which the FHSC is transparent, the radiation pressure can no longer counterbalance the increased gravitational pull, triggering another collapse. Another equilibrium is reached when the warm plasma is sufficiently dense and thereby opaque to absorb enough blackbody radiation to support itself against gravitation; this object is now called a protostar. Its radiation supplied by the kinetic energy of still-accreting material, attenuates the protostellar cloud‘s contraction and the remaining GMC‘s gravitational pull (Guszejnov and Hopkins 2016).
Since the protostar presumably emanated from a high-turbulence region, it may inherit angular momentum, resulting in a thin accretion disk, the protoplanetary disc, which is estimated to carry a few percent of the protostar‘s mass (Armitage 2011). Herbig-Haro objects, i.e. bipolar jets along with exhaust speeds of several 100 km/s along the rotational axis, are then often formed, ejecting material carrying excess angular momentum and gradually creating a thin cavity in the remaining accretion cloud. Conservation of the clouds inital angular momentum can also lead to binaries, i.e. two (proto-) stars orbiting each other.

When mass accretion is declining, the formerly steady supply of kinetic energy to the protostar is insufficient to sustain equilibrium with gravity; the protostar contracts and starts deuterium fusion[5]. The hereby released thermal energy repels the accretion cloud, making the star visible in the optical spectrum. Light protostars below $8M_\odot$ may shed their envelope before contraction suffices for hydrogen burning, resulting in a brief pre-main sequence (PMS) star phase, lasting up to 1% as long as the subsequent hydrogen burning in the main sequence.

2.1.4 Main Sequence

When the core temperature reaches 4×10^6 K, hydrogen burning (see chapter 2.2 for the fusion mechanism) sets in and provides an energy source to compensate for the radiative losses on the surface of the star. The newborn star is in equilibrium of gravity and pressure; assuming a spherical symmetry, this is expressed by the equation of hydrostatic equilibrium[6]:

$$-\frac{dp(r)}{dr} = G\frac{m(r)\rho(r)}{r^2} \tag{2.2}$$

The pressure is composed of two main components with very different behavior which has great influence on the implications of this equation: While ideal gas pressure is proportional to T, blackbody radiation pressure scales with T^4 (see Chapter 4.1), so low-mass stars are predominately stabilized by gas pressure while massive stars mostly rely on radiation pressure. From this, the luminosity can be estimated to be $L \propto M^3$ when gas pressure dominates, leading to a total hydrogen burning time $t_H \propto M/L \propto M^{-2}$, assuming constant luminosity and a fixed mass fraction of hydrogen in the initial stars. As will be discussed later, the hydrogen burning time is a good measure for the lifetime of a star. For massive stars above $20M_\odot$, the luminosity is roughly proportional to the mass; strong stellar winds caused by the high luminosity cause significant mass losses by stellar winds, so the estimation for the hydrogen burning time is not applicable.
Turbulences caused by convective energy transport, i.e. the thermal energy transported by ascending hot plasma from the inner regions, become more relevant with increasing density and thereby mass and require increased pressure to remain in equilibrium. Therefore, the results drawn from equation 2.2 underestimate the luminosity‘s growth with mass; by analyzing binaries, whose participants‘ masses can be determined by measuring their orbital periods, it was found empirically that $L \propto M^{3.7}$ for stars below $18M_\odot$ (Demircan and Kahraman 1991)[7], matching well with the empirical lifetime of $t_L \propto M^{-2.5}$. More sophisticated models, such as described by Maeder and Meynet (1988), approach these values with high precision.
As the surface temperature of the star is a function of its luminosity with $L \propto R^2T_s^4$ and the radius has both theoretically and empirically found to be a function of the mass ($R \propto M^{0.56}$ for stars above $1.6M_\odot$, Demircan and Kahraman 1991), there is a distinct relation between surface temperature and luminosity of a hydrogen fusing star, which between a mass of $1.6M_\odot$ and $18M_\odot$ is given as $L \propto T_s^{5.7}$. For the entire mass range, $L \propto T_s^6$ is often used as an estimate.
In the HRD, the area matching observed hydrogen burning stars is called the main sequence (MS). A star that just began hydrogen burning will start in the lower end of the region, the zero age MS (ZAMS) and move very little during its hydrogen burning phase, just slightly increasing in both parameters until it approaches the terminal age main sequence (TAMS). As shown in Table 2.1, most of a star‘s lifetime is spent on the main sequence, accumulating helium in its core (see Chapter 2.2).

[5]This contraction phase can make the protostar highly luminous; in this case, the object is called a T-Tauri star ($\leq 3M_\odot$) or, depending on its surface temperature, a Herbig Ae/Be star.

[6]With enclosed mass $m(r)$ so that $dm(r) = 4\pi r^2\rho(r)dr$

[7]Other studies such as Eker et al. (2015) showed different results, but did not fit the double-logarithmic data to be proportional, but rather to a linear function with an offset from zero, which would render the simple equations presented here more bulky.

burning stage	time scale	temperature [GK]	density [g/cm^3]	luminosity [$L_\odot$]
H	11 My	0.035	5.8	28000
He	2 My	0.18	1390	44000
C	2 ky	0.81	2.8×10^5	72000
Ne	0.7 y	1.6	1.2×10^7	75000
O	2.6 y	1.9	8.8×10^6	75000
Si	18 d	3.3	4.8×10^7	75000

Table 2.1: Simulated burning stages of a $15M_\odot$ star (Source: Woosley and Janka 2005).

2.1.5 Giants and Supergiants

Once the hydrogen supply in the core of a star with a mass greater than about $0.4M_\odot$ is drained, the core contracts, pulling new hydrogen supply in a region subjected to stronger gravity than before (due to the compressed core), leading to a higher fusion rate, stronger radiation and a significant expansion of the outer shells; the star becomes a red giant and moves to the corresponding branch in the HRD, jumping in luminosity by a factor of $10^2 - 10^4$. The expansion of the outer layers redistributes the energy transported to the surface to a much larger area, reducing the surface temperature to about 5000 K even though the energy output has been increased. Convection is now able to carry products from the expanded fusion zone (though not from the core) to outer layers, often referred to as the first dredge-up. Meanwhile, for stars of less than $2M_\odot$, the density of the core will be sufficient for electron degeneracy pressure to stabilise the contraction, but will induce further heating of the core, where at roughly 10^8 K helium will begin to be fused into carbon.
When the innermost part of the core, mostly supported by degeneracy pressure, reaches the same temperature, thermal runaway occurs, resulting in a rapid carbon fusion called the helium flash. High-mass stars reach the temperature at lower densities where degeneracy pressure is non-dominant, avoiding the runaway. One way or the other, the fusion process leads to further core contraction. During this phase, the luminosity changes little while the surface temperature decreases, following a horizontal path in the HRD.
Subsequently, a star of sufficient mass may enter a second red giant phase, referred to as the asymptotic giant branch (AGB) phase, where in the early stage (E-AGB) helium is fused in a shell outside of the core analogously to the first red giant phase; a carbon-oxygen core is formed, the stars radius increases drastically to up to an astronomical unit ($\approx 215R_\odot$) and appears as a red giant again. Subsequently, a repeating process occurs: the thermally pulsing AGB (TP-AGB), in which, after the helium shell is short on fuel, contraction enables an outer hydrogen shell to fuse, which in the next $10^4 - 10^5$ years accumulates a new helium shell, spontaneously igniting in another helium shell flash, which, opposing the first helium flash due to its proximity to the surface, has a drastic effect on the luminosity of the star. After several 100 years, the helium shell depletes and the process restarts. This process can mix material from the different shells of the stars, reffered to as the third dredge-up. During the thermal pulses, stellar winds are strengthening, leading to high mass losses of up to 70% of their initial mass, generating a circumstellar envelope (CSE).
Stars heavier than $9M_\odot$ accumulate enough pressure and temperature to fuse to high-order elements (see Chapter 2.2), generating an onion-like structure and are classified as red supergiants in this phase. Wolf-Rayet stars are massive stars which have shed most of their outer layers due to strong stellar winds, leaving the extremely hot ($\sim 10^5$ K surface temperature) core layers exposed. They can stem directly from massive stars or red or blue supergiants.

2.1.6 White Dwarves

If a stars mass is insufficient to ignite carbon and oxygen in the AGB phase (roughly 10^9 K required), the core will contract when fuel runs out as in the beginning of the red giant phase, quickly igniting the lower hydrogen and helium shells now dragged into higher-temperature zones, shedding its envelope in a final radiation burst. The remaining hot and extremely dense core, a white dwarf (WD), is not able to fuse nuclei and thus cools down slowly over the next billions of years, presumably turning eventually into a black dwarf.
Thermal radiation is not sufficient to support the WD from collapse; instead, it is stabilized by electron degeneracy pressure, a result of the Pauli principle: Further compression would force electrons to occupy higher energy levels. The Chandrasekhar mass limit $\lessapprox 1.46 M_\odot$ indicates the maximum mass up to which electron degeneracy pressure can counteract gravitation. As the electron degeneracy pressure is only dependent on the number of electrons, which in order to make the WD neutrally charged equals the number of protons, and the gravitational pressure is dominated by the nucleons' total mass, the Chandrasekhar mass is dependent on the ratio of neutron mass to total nucleon mass η:

$$M_{\text{krit}} \approx 1.46 M_\odot \left(\frac{2}{\eta}\right)^2 \tag{2.3}$$

As the WD has burned respectively ejected its hydrogen supplys, $\eta \geq 2$ for virtually all compositions. A model for WDs is given with Equation 2.2 and the electron degeneracy pressure $p_{\text{e.d.}} \propto \rho^{5/3}$ with mass density ρ in the nonrelativistic[8] case. If the white dwarf's mass exceeds this limit, it explodes in a thermonuclear supernova (see chapter 3.1). In the HRD, white dwarves follow a narrow path well below any stars.

2.1.7 Populations

The metallicity Z, using the astronomical convention of referring to all elements but hydrogen and helium as metals, is the ratio of metal mass to total mass of a star and has strong influence on magnetic fields and the resulting strength of stellar winds, which catapult material into space. The rate is negligible for low and medium mass stars; a star with an initial mass of $50 M_\odot$ however can lose more than half of its total mass by stellar winds. As the early universe was poor of heavy elements, high-metallicity stars are believed to have formed later on and are categorized as Population I stars. In low-metallicity Population II stars, it has been shown that low-order alpha elements (elements that are composed of helium nuclei) often are more present than iron compared to Population I stars; this indicates that Type II SNe (see chapter 3.1) had a higher influence on the composition of molecular coulds and the interstellar medium (ISM) than other supernova mechanisms. A Population III of extremely metal-poor stars is hypothetised, indicators of their existence have been indirectly observed from distant parts of the universe. The metals are denser than hydrogen and thereby accumulate near the core, which can reduce the nucleofusion rate and thereby the luminosity, particularily in the main sequence.

2.2 Nucleogenesis

Stars are powered by nuclear fusion of light elements as explained in Chapter 2.1.4. In general, fission or fusion towards iron tends to release energy, providing the necessary radiative pressure to support the star and energy to compensate for its surface radiation energy losses; as (partially) explained by the nuclear shell model, the individual reactions may however consume energy. ^{56}Fe is generally accepted as the isotope with the highest binding energy per nucleon; there are elements with higher energy such as ^{58}Fe or ^{62}Ni, but since there are no efficient production

[8] When the energy levels of the electrons are non-negligible to their rest masses, the velocities approach the speed of light, resulting in a different pressure function of $p_{\text{e.d.}} \propto \rho^{4/3}$.

mechanisms for those, their abundance and thereby influence can be neglected. The individual processes mentioned in the previous section and their dependencies will be elaborated in detail in the following.

2.2.1 Hydrogen Burning

Hydrogen burning, referring to the process of fusing helium nuclei from protons, is the main source of radiation pressure in main sequence stars. Per fused helium nucleus, 26.73 MeV are released in total; depending on the details of the reaction, this energy is shared between radiation and neutrino emissions. There are two important reaction paths supposedly dominating the fusion:
The proton-proton chain reaction starts off with the pp-reaction, in which two protons are fused and subsequently decay into deuterium, which again fuses with a proton to form ${}^{3}_{2}\mathrm{He}$. The β-plus decay from the diproton into deuterium is extremely rare and therefore dominates the reaction speed; the decay into protons is far more likely. A proton-electron-proton (pep) reaction is also possible (Bellini et al. 2012), however, the chance of this three-body collision is comparably low; in the sun, the ratio of pp/pep is estimated to be ≈ 400. From this light isotope, four different branches lead to ${}^{4}_{2}\mathrm{He}$ as shown in Table 2.2. The pp-IV reaction is as of yet purely hypothetical; the pp-I to pp-III reactions have been confirmed and run in parallel. The pp-I reaction dominates between 4-14 MK, the pp-II reaction between 14-23 MK and the pp-III reaction above 23 MK.
When sufficient abundances of carbon are present, either through the composition of the parental molecular cloud or helium burning (discussed below), it can act as a catalyst for hydrogen fusion: As it is gradually enriched with protons, occasional β^+ decays occur to optimize the proton/neutron ratio. Some transistions are strongly supressed, the reaction ${}^{15}_{7}\mathrm{N}$ ($1/2^-$) + p ($1/2^+$) $\rightarrow$ ${}^{16}_{8}\mathrm{O}$ (0^+) + 11.6 MeV for instance (with the nuclear spin denoted in brackets) is very unlikely to happen as unchanged nuclear spin forbids the excess energy to be ejected via a single photon, so kinetic energy is released instead by ejecting an α-particle as shown in the CNO-I process in Table 2.2. In this particular case however, even the supressed side branch leads to the cyclic CNO-II reaction[9]; in the Sun's core, the ratio of CNO-I/CNO-II is estimated to be $\approx 10^4$. When under high density and temperature conditions, the proton capture cross section of some nuclei may exceed the rate of the beta decay, leading to slightly altered reaction cycles, the so-called hot CNO (HCNO) cycles, which are generally slightly faster than their cold counterparts; especially the HCNO-II cycle, circumventing the limiting ${}^{14}_{7}\mathrm{N}$ proton capture, can significantly increase the helium production rate.
The positrons produced by the β^+ decays of both processes annihilate with the plasma's electrons, leading to the emission of two photons carrying a minimum total of 1.02 MeV, equalling the rest mass of the annihilated particles; their kinetic energies can add (typically minute) amounts of energy. The neutrinos can easily escape the plasma, resulting in an energy loss; in particular, the pp-III neutrinos carry an average of 28% of the released energy.

2.2.2 Helium Burning

Two colliding α-particles can fuse to the unstable ${}^{8}_{4}\mathrm{Be}$; if this isotope collides with a third α-particle, this results in a stable ${}^{12}_{6}\mathrm{C}$ nucleus, releasing 7.27 MeV per carbon nucleus. Analogously to the CNO-II process, this should be strongly supressed because the nuclear spin is unchanged, yet coincidentially, the energies of the helium and beryllium nuclei as well as a resonance of the ${}^{12}_{6}\mathrm{C}$ nucleus match to a high degree[10]. The subsequent fusion reactions of ${}^{16}_{8}\mathrm{O}$ and ${}^{20}_{10}\mathrm{Ne}$ are

[9] There are two more cold CNO cycles mostly occuring in massive stars, each being a suppressed alternative to the α-ejection of the respectively previous. Correspondingly, there is a third hot CNO cycle.

[10] Naturally, the energies are not identical, but scaled with the quantities of nuclei in the reaction. Each product has slightly higher energy than its educts; their kinetic energy provides the difference.

name	reaction	rate
proton-proton chain reactions		$\propto T^4\rho$
H$\rightarrow {}^3_2$He		
pp	$2\mathrm{p} \rightarrow {}^2_2\mathrm{He} \xrightarrow{\beta^+} {}^2_1\mathrm{D} \xrightarrow{+\mathrm{p}} {}^3_2\mathrm{He}$	
pep	$2\mathrm{p} \xrightarrow{e.c.} {}^2_1\mathrm{D} \xrightarrow{+\mathrm{p}} {}^3_2\mathrm{He}$	
${}^3_2\mathrm{He} \rightarrow {}^4_2\mathrm{He}$		
pp I	$2\ {}^3_2\mathrm{He} \rightarrow {}^4_2\mathrm{He} + 2\mathrm{p}$	
pp II	${}^3_2\mathrm{He} + {}^4_2\mathrm{He} \rightarrow {}^7_4\mathrm{Be} \xrightarrow{e.c.} {}^7_3\mathrm{Li} \xrightarrow{+\mathrm{p}} 2\ {}^4_2\ \mathrm{He}$	
pp III	${}^3_2\mathrm{He} + {}^4_2\mathrm{He} \rightarrow {}^7_4\mathrm{Be} \xrightarrow{+\mathrm{p}} {}^8_5\mathrm{B} \xrightarrow{\beta^+} {}^8_4\ \mathrm{Be} \rightarrow 2\ {}^4_2\ \mathrm{He}$	
pp IV	${}^3_2\mathrm{He} + \mathrm{p} \xrightarrow{\beta^+} {}^4_2\mathrm{He}$ (hypothetical)	
CNO cycles		$\propto T^{17}\rho$
CNO-I	${}^{12}_6\mathrm{C} \xrightarrow{+\mathrm{p}} {}^{13}_7\mathrm{N} \xrightarrow{\beta^+} {}^{13}_6\mathrm{C} \xrightarrow{+\mathrm{p}} {}^{14}_7\mathrm{N} \xrightarrow{+\mathrm{p}} {}^{15}_8\mathrm{O} \xrightarrow{\beta^+} {}^{15}_7\mathrm{N} \xrightarrow{+\mathrm{p}} {}^{12}_6\mathrm{C} + {}^4_2\mathrm{He}$	
CNO-II	${}^{14}_7\mathrm{N} \xrightarrow{+\mathrm{p}} {}^{15}_8\mathrm{O} \xrightarrow{\beta^+} {}^{15}_7\mathrm{N} \xrightarrow{+\mathrm{p}} {}^{16}_8\mathrm{O} \xrightarrow{+\mathrm{p}} {}^{17}_9\mathrm{F} \xrightarrow{\beta^+} {}^{17}_8\mathrm{O} \xrightarrow{+\mathrm{p}} {}^{14}_7\mathrm{N} + {}^4_2\mathrm{He}$	
HCNO-I	${}^{12}_6\mathrm{C} \xrightarrow{+\mathrm{p}} {}^{13}_7\mathrm{N} \xrightarrow{+\mathrm{p}} {}^{14}_8\mathrm{O} \xrightarrow{\beta^+} {}^{14}_7\mathrm{N} \xrightarrow{+\mathrm{p}} {}^{15}_8\mathrm{O} \xrightarrow{\beta^+} {}^{15}_7\mathrm{N} \xrightarrow{+\mathrm{p}} {}^{12}_6\mathrm{C} + {}^4_2\mathrm{He}$	
HCNO-II	${}^{15}_8\mathrm{O} \xrightarrow{\beta^+} {}^{15}_7\mathrm{N} \xrightarrow{+\mathrm{p}} {}^{16}_8\mathrm{O} \xrightarrow{+\mathrm{p}} {}^{17}_9\mathrm{F} \xrightarrow{+\mathrm{p}} {}^{18}_{10}\mathrm{Ne} \xrightarrow{\beta^+} {}^{18}_9\mathrm{F} \xrightarrow{+\mathrm{p}} {}^{15}_8\mathrm{O} + {}^4_2\mathrm{He}$	
triple-α process		$\propto T^{40}\rho^2$
	${}^4_2\mathrm{He} \xrightarrow{+\alpha} {}^8_4\mathrm{Be} \xrightarrow{+\alpha} {}^{12}_6\mathrm{C}^* \rightarrow {}^{12}_6\mathrm{C}\ \left(\xrightarrow{+\alpha} {}^{16}_8\mathrm{O} \xrightarrow{+\alpha} {}^{20}_{10}\mathrm{Ne}\right)$	
Intermediate element burning		
C burning	$2\ {}^{12}_6\mathrm{C} \rightarrow {}^{20}_{10}\mathrm{Ne} + \alpha$ or ${}^{24}_{12}\mathrm{Mg}$ or others	
Ne burning	${}^{20}_{10}\mathrm{Ne} \xrightarrow{+\lambda} {}^{16}_8\mathrm{O} + \alpha$ or $\xrightarrow{+\alpha} {}^{24}_{12}\mathrm{Mg}$	
O burning	$2\ {}^{16}_8\mathrm{O} \rightarrow {}^{28}_{14}\mathrm{Si} + \alpha$ or others	
α-ladder		
Si burning	${}^{28}_{14}\mathrm{Si} \overset{\pm\alpha}{\rightleftharpoons} {}^{32}_{16}\mathrm{S} \overset{\pm\alpha}{\rightleftharpoons} {}^{36}_{18}\mathrm{Ar} \overset{\pm\alpha}{\rightleftharpoons} {}^{40}_{20}\mathrm{Ca} \overset{\pm\alpha}{\rightleftharpoons} {}^{44}_{22}\mathrm{Ti}$ $\overset{\pm\alpha}{\rightleftharpoons} {}^{48}_{24}\mathrm{Cr} \overset{\pm\alpha}{\rightleftharpoons} {}^{52}_{26}\mathrm{Fe} \overset{\pm\alpha}{\rightleftharpoons} {}^{56}_{28}\mathrm{Ni} \overset{\pm\alpha}{\rightleftharpoons} {}^{60}_{30}\mathrm{Zn}$	
Neutron sources		
Main	${}^{13}_6\mathrm{C} \xrightarrow{+\alpha} {}^{16}_8\mathrm{O} + \mathrm{n}$	
Weak	${}^{22}_{10}\mathrm{Ne} \xrightarrow{+\alpha} {}^{25}_{12}\mathrm{Mg} + \mathrm{n}$	

Table 2.2: Overview of stellar nucleofusion processes. Electron and neutrino products and educts of decay reactions as well as photons are omitted in the reaction notations.

suppressed because of the nuclear spin as well as the increasing coulomb barrier of the nuclei. The half-life of ${}^{8}_{4}\mathrm{Be}$ is $\approx 7 \cdot 10^{-17}$ s, so the process requires high temperature and density to procude carbon at a significant rate. The reaction speed scales with the 40th power of temperature and the square of density, being far more sensible to changes in these parameters as photon-photon chain reactions and CNO cycles. Because of this, the triple-α process is negligible on the main sequence, but can contribute significant energy during the red giant phase.

2.2.3 Intermediate Element Burning

The large abundances of carbon produced by helium burning are unlikely to fuse with α-particles or neutrons. While fusion with protons leads to a CNO cycle, heavier elements (apart from those in the CNO cycles) are primarily produced by carbon fusing with itself. Along the small amounts of ${}^{16}_{8}\mathrm{O}$ that were produced during the helium burning, this leads to a O-Mg-Ne core composition. While magnesium under these conditions is comparably inert, the temperature increase caused by the core contraction when the carbon burning is coming to an end enables blackbody photodisintegration of neon to oxygen, thereby releasing fast α-particles which may fuse with other neon nuclei to magnesium. After a few years, the decreasing reaction rate causes the now predominately O-Mg core to contract again, enabling oxygen burning. This again is a homonuclear process, meaning that the most likely reaction is the fusion of oxygen with itself, resulting in large abundances of ${}^{28}_{14}\mathrm{Si}$ as shown in Table 2.2.

2.2.4 The α-Ladder

After the energy supply from oxygen burning decreases, the burning process is now again powered by α-particle capture. However, the very high temperatures necessary to generate a relevant cross section also lead to photodisintegration; the higher-order α-elements (i.e. elements composed of α-particles with ${}^{4n}_{2n}\mathrm{X}$ nuclei) are in a quasi-equilibrium of being created and destructed. The entire process is commonly referred to as silicon burning and lasts about one day until the resources are depleted and the core collapses.
This process is still relevant after the end of the stars lifetime; in SNe, explosive silicon burning during the SN and later an α-rich freeze-out during the SNRs plasma cooling may redistribute the spatial and ratiometric distribution of the heavy α-elements.

2.2.5 Nucleon Capture

The increased charge of heavy elements lowers the probability of an α-particle to overcome the coulomb barrier. Elements heavier than nickel[11] are therefore believed to be primarily produced by neutron capture.
In stars, the main neutron sources are the two processes depicted in Table 2.2, the main component being dominant in low-mass AGB stars, the weak component employing the neon produced in the carbon burning of massive stars. Under typical conditions in stars, the eponymous cross section of neutron capture exceeds the average β^- decay half-time of resulting unstable nuclei, so repeated occurence of both processes, the so-called slow- or s-process, result in a fusion path travelling tangentially to the stable nuclei in the chart of nuclides. This process typically fuses elements roughly up to strontium, low metallicity stars however, having an increased lifetime because of their bigger fuel supplies, may fuse elements up to lead.
During a CC-SN, a massive number of neutrons is released in short time; furthermore, β^- decay is strongly supressed nearby the proto-NS by electron degeneracy pressure. Both effects in conjunction result in the rapid- or r-process, a fast fusion of extremely neutron-rich unstable

[11] Even though the general trend of heavier elements is to have less nuclear binding energy, the rest mass of the neutron has to be considered as well, rendering neutron capturing reactions exothermic in many cases.

elements, typically only decaying if a magic neutron number (such as 50, 82, 126) is reached. This may result in nuclei up to $A \approx 260$, where fission may occur and feed them back into the neutron accumulation path.
Both processes, neither being definitely proven, yet possible and widely accepted in the scientific community, result in neutron-rich isotopes. The origin of the terrestial abundances of neutron-poor isotopes however is still unclear; hypothesized proton capture in CC-SNe were disproven[12], rapid proton capture processes may occur during hydrogen flashes in binaries with at least one neutron star involved.

3 Supernovae and their Remnants

3.1 Supernova Mechanisms

3.1.1 Thermonuclear Supernovae

When a WD is in a binary with another star, meaning that the two are orbiting each other, it may start accreting material gravitationally. If the WD approaches the Chandrasekhar mass limit, electron degeneracy pressure offers less support, the WD starts carbon and oxygen burning. Due to the high density, no effective radiative cooling is possible. The core temperature rises, making fusion of heavier elements possible, thermal runaway ensues and results in large parts of the WD's mass to be synthesized to ^{56}Ni. Within a few seconds after carbon burning started, energy in the order of 10^{51} erg (= 1 B, "Bethe"), equivalent to the binding energy of the WD, is released, resulting in a shockwave disrupting the dwarf. It is also possible that the high gravity on the WD's surface ignites the accreted matter to a degree where the (typically inhomogeneously accreted) matter causes density variances in the WD so that local thermal runaway heats the WD sufficiently to cause an explosion well below the Chandrasekhar mass.
The binary may originate as two stars with slightly different mass. Because these are likely to have been born from the same cloud collapse, their age can be estimated to be roughly equivalent. Because of this, the heavier partner turns into a red giant first. The radius of the outer shells may now well be in the magnitude of the distance between the stars. Due to the gravitational pull of the lighter star, the outer shell will start to engulf both partners and form a thin disk in the plane of the rotation, which carries a significant amount of the total angular momentum and may be shed during the process, leaving the heavier stars core (a WD once nucleogenesis has ceased) exposed; the stars however now rotate slower around each other, causing a decreased distance and making accretion to the surface of the WD possible. Also, collisions or binaries of two white dwarves are a possible origin of Type Ia SNe, although believed to be far less common.

3.1.2 Core Collapse Supernovae

Once the cores composition is dominated by iron or the heaviest element the respective star can synthesize, radiative pressure can no longer support the star. Therefore, the core is only stabilised against its own gravitational pull by the degeneracy pressure of electrons, similar to a WD. Above the respective Chandrasekhar limit (for a hypothetical pure $^{56}_{26}$Fe core about $1.26 M_\odot$, see Equation 2.3), this can no longer be sustained and the core collapses, releasing thermal gamma rays which cause photodisintegration of the iron atoms, resulting mostly in helium nuclei and free neutrons. Given the high electron density, the inverse β-decay occurs in abundance, converting electrons and protons into neutrons and antineutrinos; as the latter only interact weakly, they can pass the core and the surrounding matter, thus transporting energy out of the star and reducing the degeneracy pressure that otherwise would be slowing down the

[12] Given the assumed maximum proton densities in CC-SNe, low temperature environments would result in an insufficient cross section while high temperature environments would photodisintegrate unstable nuclei faster than they would be created.

collapse. When a majority of protons have converted into neutrons[13], the densities upper limit is given by the neutron degeneracy pressure and comparable to the density in an atomic nucleus. Neutron degeneracy pressure suddenly stops the collapse, resulting in a neutron star (NS) with an initial temperature in the order of 10^{11} K and a diamater of about 20 km. Neutrinos still trapped in the core travel slowly to the surface, thus releasing the thermal energy gradually. If however, especially for stars heavier than $20M_{\odot}$, neutron degeneracy pressure does not suffice to stabilise the NS, no other force (apart from hypothetical quark degeneracy pressure, predicting the existence of strange quark stars) can withstand the gravitational pull, resulting in the collapse into a singularity, a black hole (BH). Also, some SNe as described in the following may disrupt their former cores during the explosion, leaving no compact central object (CCO) behind.
The collapse of the core occurs in a timescale of milliseconds and with relativistic velocities up to $\beta = 0.23$, far greater as the speed of sound in the surrounding layers. Their subsequent collapse follows the core reluctantly and is slowed down by collision with inner layers rebounding from the nearly incompressible NS, heating up the infalling material in the process. However, the energy of the rebound is insufficient to induce explosion; the expansion stalls. Due to the short time range, this works equally with a non-stable NS that eventually collapses into a BH as the neutron degeneracy pressure dampens the NS collapse substantially. It is suspected that an as of yet poorly understood process transfers energy from the escaping neutrinos to the rebounding matter; roughly 1% of the energy released during core collapse would suffice to trigger explosion. Some stars however do not explode at all, with a blurred empirical mass of $8M_{\odot}$ required for triggering an SN; otherwise, a WD remains.
In contrast to WDs, stars vary widely in mass and composition; compared to thermonuclear SNe, a diversity of other processes may affect the explosion as described in the following.

Electron Capture Supernovae. For comparably low-mass stars ($8 - 10M_{\odot}$), the gravitational pressure is insufficient to fuse an iron core; during their red giant phase, the cores are primarily composed of oxygen, neon and magnesium. Above the critical density limit of $4 \cdot 10^{12}$ kg m^{-3} is exceeded, the cross section of the magnesium nuclei capturing electrons from the surrounding plasma in an inverse β-decay becomes efficient, reducing number of electrons and thereby the electron degeneracy pressure and leading to the cores collapse into a NS (Takahashi et al. 2013). The explosion continues as in the general case described above.

Pair Instability Supernovae. The interaction of high-energy photons with nuclei, electrons or other photons may cause electron-positron pair production, reducing the number of high energy photons in the process. In the inner layers of very massive stars (above $\approx 140M_{\odot}$), the plasma can be sufficiently hot that the radiation pressure caused by blackbody radiation is annihilated to a considerable degree through this process. Gravitational pressure and radiation pressure are no longer in equilibrium; the core contracts, heating up further and thereby increasing the rate of pair production, resulting in a thermal runaway reaction. Within a few seconds, the now greatly increased nucleofusion rates lead to the explosion. Characteristically, pair instability supernovae leave no remnant[14] behind as it presumably is disrupted by turbulences caused by the rapid contraction.

Photodisintegration Hypernovae. At even higher photon energies than required for pair production (therefore present in even more massive stars above $\approx 250M_{\odot}$), photons may excite atomic nulcei which subsequently emit a nucleon or an α-particle. As this is an endothermic

[13]The Brown-Bethe mechanism proposes a different solution of state for neutron stars, in which K^- mesons neutralize the protons‘ charge, with the superflous electrons being ejected. The kaons form a bose condensate which strongly attracts nucleons, thereby lowering the total energy; because of this, electron capture would be energetically unfavorable (Brown and Bethe 1994).

[14]As went unnoted with other SN types, a nebula of former stellar material forms after every kind of SN.

reaction for nuclei lighter than iron[15], the radiation pressure is reduced; collapse ensues in a similar manner to pair instability SNe. Naturally, pair production also contributes to this process. Since the core contraction and nucleofusion occurs at an even more extreme rate than in a pair instability supernova, the released kinetic explosion energy may exceed the average SN's energy of 1 B by orders of magnitude; because of this, this type of explosion is often referred to as a hypernova[16].

3.2 Classification of Supernovae

Historically, in the absence of deeper understanding of the underlying processes, supernovae have been classified according to their spectral lines and shape of their light curve (the total luminosity as a function of time) as shown in Figure 3.1.

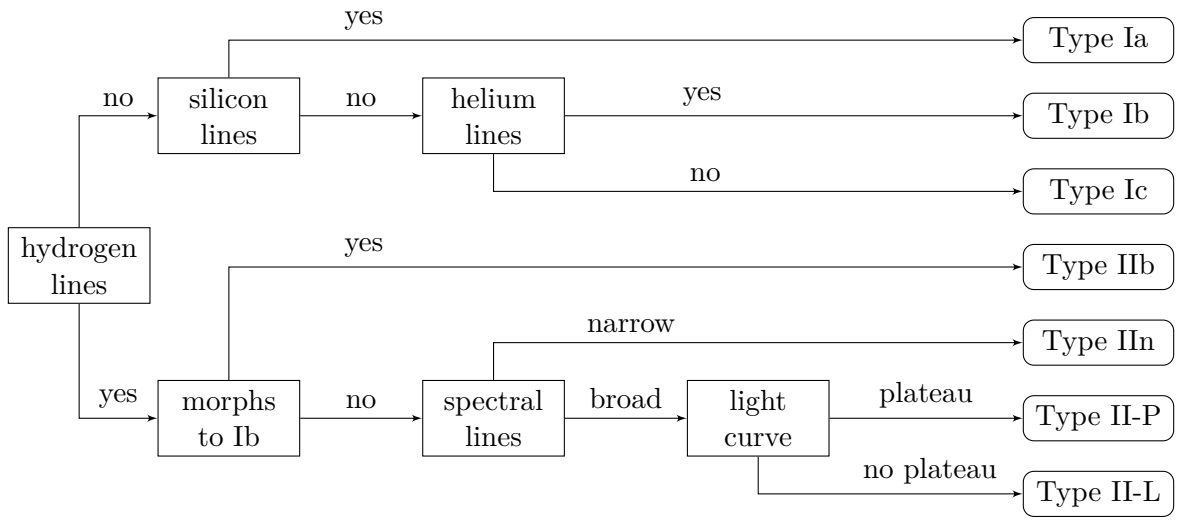

Figure 3.1: Observation-based classification of supernovae. See text for detailed description.

Type Ia SNe have very homogeneous photometric and spectroscopic signatures, which led to the general agreement that they are the result of the equally homogeneous thermonuclear SNe (Branch et al. 1995). The absence of hydrogen lines matches with this assumption since the WDs from which thermonuclear SNe emerge have ejected their hydrogen shells long ago so that they can be presumed to have mixed with the ISM; the hydrogen of a companion star was the first to be accreted on the WD surface and fused by the high impact temperatures caused by the WDs strong gravitational field.
Unlike other SN types, they appear to occur in all types of galaxies; this in combination with their comparably high average luminosities make them a good indicator for the geometry of the universe as a strong correlation between peak luminosity and light curve decay was found[17] (Phillips 1993): The second-order Phillips equation, with the decline in observed brightness $\Delta m_{15}(B)$ and the Hubble constant H_0, was reported to achieve a precision of 0.1 magnitudes (see Chapter 4.2) for the SNe associated with regular Type Ia behavior (Jha et al. 2007):

$$M_{max} = -19.504 + 0.736\Delta m_{15}(B) + 0.182\Delta^2 m_{15}(B) + 5\log H_0 \tag{3.1}$$

[15]The emitted particle can exert pressure on the outer layers similarily to photons, so its kinetic energy still contributes to the hydrostatic equilibrium; the lost energy thereby is roughly equal to the difference in binding energy between the two nuclei.

[16]Other hypernova mechanisms exist; pair instability SNe of high-mass stars may equally be dubbed hypernova.

[17]The distance of the examined set of SNe, necessary for the conversion from relative magnitude to luminosity as described in Chapter 4.2, was approximated by determining the distance of the galaxies in which they are contained with methods like surface brightness fluctuation measurement or the Tully-Fisher relation, who will not be further explained in this thesis. For more informations, see (Jacoby et al. 1992).

However, there are subcategories of Type Ia which do not fit in this spectrum, such as for instance the bright super-Chandrasekhar mass SNe and the faint Types .Ia and Iax, which are hypothetised to be the result of two white dwarves colliding (Kamiya et al. 2012) and binaries of two white dwarves (Bildsten et al. 2007) respectively. These SN types may exhibit similar spectra and thus can be hard to differentiate, so the Phillips equation is to be treated with care as a mere suggestion, while other observables are more reliable indicators of distance.
All other SN Types are accepted to be the result of CC-SNe with different progenitor masses and metallicities as well as different explosion mechanisms (Heger et al. 2003) as shown in Table 3.1, along with the more exotic CC mechanisms discussed above. The lightest non-electron capture SNe typically exhibit light curves with extended plateau, corresponding to being Type II-P SNe; as the decay rates for the radioactive ^{56}Ni and its daughter nucleus are short compared to other radioactive α-elements (see Chapter 6.2 for a representative juxtaposition), a high abundance of radioactive nickel would lead to a high initial luminosity, but a short decay; this is coherent with the tendency of light stars to produce a smaller ratio of heavy isotopes. Coherently, a higher metallicity with a progenitor of the same mass can result in a more quickly decaying luminosity peak, corresponding to Type II-L.
An alternative explanation would be the mediocre ejection velocity of the hydrogen envelope during the red giant phase, causing it to be still nearby and dense when the shock front arrives (see Chapter 3.3). The subsequent ionisation results in a high opacity around the remnant, reducing the intensity of the initial light curve. When the hydrogen has cooled down sufficiently, recombination restores the transparency, giving the appearance of a flat lightcurve. This is supported by the option of pair instability SNe to display II-P spectra, as the accelerated evolution leaves less time for the envelope to escape.
More massive progenitors, having ejected their hydrogen envelopes with higher velocities during the red giant phase due to their higher luminosities applying more radiation pressure, often show little hydrogen lines, indicating that the ejected hydrogen has been dispersed in the ISM, resulting in Type Ib and Ic explosions, the absence of silicon lines being due to the high temperatures throughout the stars' volumes enabling heavier elements even in outer shells.
In between these extremes, Type IIb SNe are found, which initially exhibit weak hydrogen lines, but subsequently change their spectrum to rather resemble a Type Ib SN. The causes for this are uncertain; in a binary system of unequal stars, the bigger one, having ejected its envelope with a core predominately composed of helium, may have exploded while the smaller one still carried significant amounts of hydrogen.

cause	mass [$M_\odot$]	metallicity	SN	CCO
electron capture	8-10	/	II-P (faint)	NS
core collapse	10-25	/	II-P (faint)	NS
	25-40	low-solar	II-P	NS→BH
		high	II-L/IIb	NS
	≥40	near solar	Ib/Ic (faint) or GRB[18]	NS→BH
		very high	Ib/Ic	NS
	90-140	low	none/GRB	BH
pair instability	140-250	low	II-P/hypernova/GRB	none
photodisintegration	≥ 250	low	none/GRB	BH

Table 3.1: Presumed progenitors of SN types (Source: Heger et al. 2003)

[18] A gamma ray burst (GRB) is a comparably short ($\lessapprox$ 200 s) boradband pulse of extremely high energy.

3.3 Evolution of Supernova Remnants

3.3.1 Post-Supernova Nucleogenesis

After the supernova has taken place, two distinct phases may remain: A dense compact central object (CCO) from the NS that reflected infalling matter during the explosion on the one hand and matter fast enough to escape the CCO's gravitational field, the so-called ejecta, on the other. For understanding the ratios of elements and their isotopes in the universe, it is insufficient to determine in which abundances they are produced during the various forms of a star's life (and also during the SN, see below), but also the ratio in which they are either ejected or trapped and disassembled in the remaining NSs and BHs, given by so-called mass cut.
As Figure 3.2 shows on the left, the relative ejected elemental abundances are correlated by their production site. This is helpful in simulations aimed to estimate elemental yields as a function of progenitor mass because the mass cut can be adjusted to fit observational tendencies; for instance, the correlation shown in Figure 3.2 on the right was adjusted to fit observed correlations between progenitor mass and ^{56}Ni yield.
Heated by the collision with NS or outer layers, substantial nuclear transformations still occur in the ejecta, first and foremost silicon burning which modifies the ratio of the α-elements as described in Chapter 2.2.4. Once the plasma starts cooling, the average kinetic energy of free α-particles does not suffice anymore for some isotopes to be fused, while nucleofission of the same nuclei, either by collisions or photodisintegration, is still relevant. The abundance of helium nuclei grows as they gradually run out of reaction partners, wherefore this process is often referred to as "α-rich freeze-out".
A typical isotope produced primarily by this mechanism is the radioactive α-titanium mentioned above; as will be shown in Chapter 6.2, it is well-fit for quantitative measurement; comparison with empirically constrained abundances of the early light curve dominating α-nickel in combination with simulated mass cuts therefore gives valuable insight in the reactive aspect of SNR evolution.

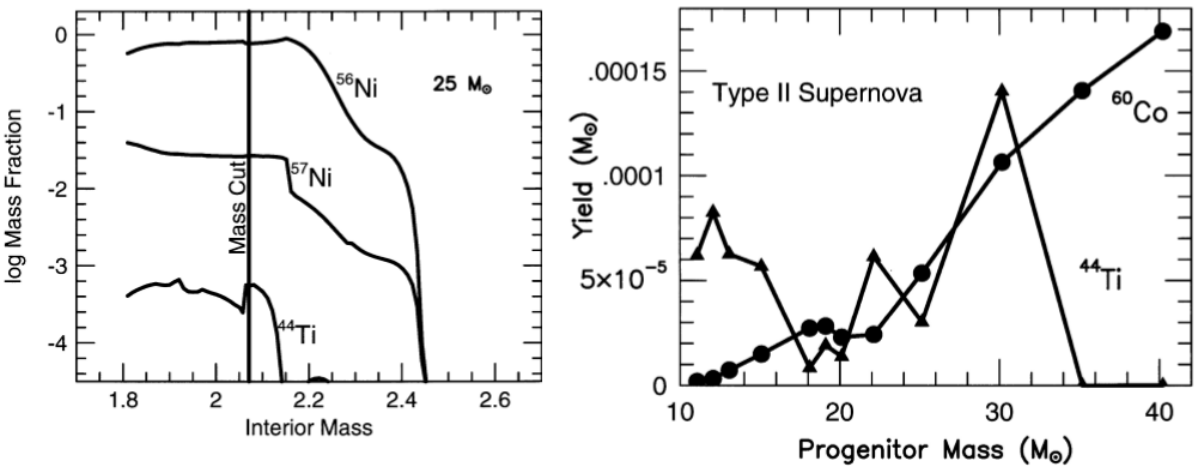

Figure 3.2: Comparative yields of ^{44}Ti(Source: Diehl and Timmes 1998). *Left:* Simulated distribution of ^{44}Ti, ^{56}Ni and ^{57}Ni inside of a $25M_\odot$ star. The interior mass expresses the radial position in terms of enclosed mass, the mass cut represents the radius above which the nuclei are ejected (though they may fall back on the NS during the explosion). *Right:* Simulation of ^{44}Ti and ^{60}Ni yield in a Type II SN (subcategory not specified) with a mass cut derived from ^{56}Ni observations.

3.3.2 Remnant Kinematics

The evolution of the supernova remnant is dominated by the accretion of circumstellar matter (CSM), i.e. the (plasma) contents of the stellar wind bubble in the early phase and the ISM in the late phase. It can be roughly modelled by four phases (e.g. Woltjer 1972; Gull 1973):

Phase I: Free Expansion. While the swept-up CSM is negligible in mass compared to the SNR, the expansion of the ejecta is unobstructed, so the expansion speed is approximately constant with a maximum of typically 10^7 m/s. The average particle speed in the CSM is typically below 10^4 m/s, the speed of sound magnitudes below, so the CSM is not compressed and heated until the shock front arrives; the accreted CSM mass can be assumed to be exactly the CSM mass prior to the SN within the shock front radius. The high density in this phase causes most radiation to be reabsorbed into the ejecta, so the kinetic energy of typically 1 B is roughly constant. This phase lasts typically several 100 years.

Phase II: Adiabatic Expansion (Sedov-Phase). When the accreted CSM mass approaches the magnitude of the ejecta mass, the expansion velocity decreases with roughly $v \propto t^{-1}$ while the product R^3v^2 with shock radius R remains constant in first approximation, neglecting magnetic fields, pressure of cosmic rays and inhomogenities of ISM as well as angluar asymmetries. Inside of the shock sphere, density decreases and temperature increases towards the center. Radiative losses increase as the overall density and with it photoreabsorption decreases, but are still negligible comparable to total energy in this phase, which therefore stays approximately constant; the expansion is adiabatic. The CSM encountering the shock front is heated and compressed and thus applies force to the ejecta, converting kinetic energy to thermal energy.
This causes a secondary shockwave in the ejecta, referred to as the reverse shock (RS). Note that the absolute RS radius may decrease or increase; the name implies only that it veers away from the forward shock (FS) front. The RS-heated ejecta, the so-called shocked plateau, inject significant amounts of radiation into the shock front, attenuating its deceleration by the accreted CSM.
The ejecta that have not yet encountered the RS, commonly called unshocked ejecta (even though they of course have been shocked by the initial SN blast wave) continue to be in free expansion, so the phase transistion unfolds from outside to inside. This phase lasts typically several 10^4 years.

Phase III: Momentum Conserving Expansion (Snowplow Phase). After multiple $100M_\odot$ of ISM have been swept up, the inner ejecta have cooled down to a degree where their radiative support of the forward shock is negligible; the FS is now mechanically pushed by the accumulating inner layers. The density peak at the FS intensifies, with a significant fraction of the total mass found near the outermost radius; this leads to a high electron density which stimulates recombination (see next chapter) and thereby makes radiative losses significant, cooling the ejecta mass at comparably high rate, hence the snowplow analogy. As the expansion now is close to a purely mechanical process, the momentum is conserved, so the deceleration is only dependent on the CSM density and the total mass of ejecta and accreted material. This phase lasts typically about 10^5 years and accretes ISM in the order of $4000M_\odot$.

Phase IV: Dispersal. When the expansion velocity drops into the magnitude of the ISMs brownian motion speed of $\approx 10^5$ m/s, the remnant becomes indistinguishable from the ISM.

4 Observation of Supernova Remnants

4.1 Observables

Historically, the energy spectrum of photons has been divided into different energy regimes as shown in Table 4.1 along with characteristic observables in the range. Neither are set in stone; while the definitions of the energy domains are vague, the observables merely give an overview of typical features recorded in the respective regimes.

name	radio	infrared	optical	UV	X-ray	γ
range	<1 mm	1 µm-1 mm	0.1-1 µm	1-100 eV	0.1-100 keV	> 100 keV
observables	free-free	recombination				decay
	blackbody				synchrotron	

Table 4.1: Excerpt of a categorized electromagnetic spectrum and characteristic observables.

Blackbody Radiation. A hypothetical perfect absorber, a so-called blackbody, emits a continuous spectrum depending only on its temperature. At long wavelengths, it slopes with $P \propto \lambda^{-2}$; at higher energies, the emissions drop rapidly. The resulting peak of the spectrum is given by Wien's displacement law, while the total energy flux per area is given by the Stefan-Boltzmann law:

$$T_s = \lambda_{\max}^{-1} \cdot 2.9\text{mm} \cdot \text{K} \quad \text{(Wien)} \quad ; \quad \vec{j} \propto T_s^4 \quad \text{(Stefan-Boltzmann)} \tag{4.1}$$

Stars and white dwarves have been observed to deviate only slightly from their blackbody spectrum, making their effective temperature (the one obtained from a blackbody fit) a good measure for their surface temperature.

4.1.1 Recombination Lines.

In a plasma, electrons spontaneously leave the atomic bonds or recombine to an extent given by the plasma's electron density and the nuclei involved. When recombining, they are likely to descend step by step through the orbitals in a typical time scale of $t_{n+1,n} \approx n^5 \cdot 189$ ps with n being the principle quantum number, emitting numerous photons of different energies. The energy levels of the nuclei are dependent on their ionisation; for example, the energy difference for a $L \to K$ transistion of neutral Fe averages at 6.3 keV depending on the azimuthal quantum number, while removing one electron shifts this to about 6.6 keV. Herein, the ionisation state $-q$ of nucleus X is denoted as [X $q+1$] in roman numerals, so the example above is written as [FeII]. The increase in energy can be naively depicted as the lessened shielding of the nucleus' charge by the other hull electrons making the "distance" differences of the energy levels more influential. The isotope of the particular element however barely influences the transistion energies.
Excitation and deexcitation may also be caused by collisions; if those are neglectable, the electron density in the plasma can be deduced by line ratios[19] of the same ionisation state. Besides being an important observable, recombination emission is an important part of a remnant's radiative cooling process. They are typically found throughout the infrared, optical and X-ray domain. In general, fine structure plays a minor role in astronomy[20].

[19] The probabilities for the individual spontaneous transistions independent of environmental conditions are given by the Einstein A coefficients; however, these are often not precisely known.

[20] A notable exception is the rare hyperfine spin flip of HI (atomic hydrogen) whose 21 cm emission plays a decisive role in measuring hydrogen properties in the ISM.

4.1.2 Radioactive Decay Lines.

The α-ladder (see Chapter 2.2.4) produces a variety of radioactive nuclei. As radioactive decay is a purely nuclear process and only minutely affected by ambient conditions, its γ emissions are an excellent measure for the abundance of isotopes if their mean decay time is known with sufficient precision and the radiation is strong enough to compensate its stochastic nature.
A young and thereby dense remnant can absorb some of these high energy photons and convert them to thermal energy which in return increases blackbody radiation and recombination lines; as mentioned at various points within this thesis, especially the fast-decaying and typically abundantly produced ^{56}Ni isotope is often responsible for the bulk of a remnant's early broadband emissions.

4.1.3 Bremsstrahlung.

When a charged particle is accelerated[21], photons are emitted. These continuum emissions are called bremsstrahlung and may occur in SNRs through different processes:
Thermal free-free radiation is caused by the random brownian motion of charged particles in a plasma. As electrons are much lighter than any nuclei, their emissions dominate the spectrum. The acceleration furthermore depends on the charge of the surrounding ions, making analytical treatment of the spectrum very complex; typically, the emission spectrum is either approximated by a power law function, or, when detailed information about the plasma composition is available, simulated.
Non-thermal free-free radiation is generated similarily if the plasma is not in local thermodynamic equilibrium; this does not only imply directed movement, but can also to lead turbulences. These cause complex magnetic fields, which make the spectrum even more unpredictable; it often is similar to a hard power law ("hard" implying an exponent $\gg 1$). Depending on the opacity of the plasma, both types of free-free radiations can significantly contribute to radiative cooling.
When accelerating electrons perpendicular to their velocity vector, a photon is emitted in the same direction. For relativistic electrons, the photon is additionally Doppler shifted by its Lorentz factor; atop of that, relativistic length contraction further boosts its energy by the same factor, which may result in emissions in the X-ray range. Relativistic electrons are either found in extremely hot plasma, as not typically found in an SNR remnant, or are cosmic rays accelerated by strong magnetic fields as found in pulsars. These so-called synchrotron emissions are associated with large-scale magnetic fields in contrast with free-free radiation, where the electrons are accelerated by the ions' electric fields.

4.2 Analytical Methods

Magnitude and Extinction. As defined in Chapter 2.1.2, the luminosity is the total radiative output of a star. Depending on the context, the bolometric (meaning integration over the entire energy range) absolute magnitude M_{bol} is preferred instead, being defined (with reference values from the Sun, in particular $M_{\odot\mathrm{bol}} = 4.83$) as:

$$M_{\mathrm{bol}} - M_{\odot\mathrm{bol}} = -2.5 \log \left(\frac{L}{L_\odot} \right) \tag{4.2}$$

Counterintuitively, a higher magnitude implies a lower brightness. The analogously defined absolute optical magnitude M_V represents the same in the visual spectrum. In the Milky Way, the relative optical magnitude m_V, representing the perceived brightness from an observer in the distance d in pc, is related to M_V as follows:

$$m_V = M_V - 5\,(1 - \log d) \tag{4.3}$$

[21] This refers to any change in the expected value of the velocity vector, even if its length remains unchanged.

This does not only account for the reduced solid angle, but also to the scattering caused by the ISM. As the ISM is irregular in density, Equation 4.3 is just an approximation; for precise analysis, the distance term is replaced by extinction coefficient A_V:

$$m_V = M_v - A_V \tag{4.4}$$

The extinction coefficient however only is valid for a limited energy band; furthermore, in the optical band, the extinction of individual wavelengths differ due to frequency-dependent Rayleigh scattering, resulting in a lower extinction for higher wavelengths[22], the so-called reddening. This can be used to estimate A_V when having a source in the optical with a known emission spectrum; often, the Hα/Hβ line emission ratio, the Balmer decrement[23], is used for its stability in ratio (~ 2.85) under different ambient conditions.

Doppler Mapping. Movement of light-emitting matter relative to the observer causes a Doppler shift in the spectrum. With a positive β indicating movement towards the observer, this can be expressed as $\Delta f = \beta f_0$. This in combination with line emissions from recombination or decay establishes the option to determine velocity on the observational axis. As discussed in Chapter 3.3, (ideal) early SNRs are in free expansion, giving opportunity to convert their movement to a relative position. As the ejecta expand with intially up to 10^7 m/s, the average size of an NS of 10^4 m is irrelevant and a point-like expansion center can be assumed. In the Sedov-phase however this is not trivially given; a simulation by Truelove and McKee (1999) showed that Doppler-Position mapping is no longer applicable for the shocked ejecta as shown in Figure 4.1 as the velocity-position distribution is no longer unambiguous, so any attempt of 3D mapping must be reviewed critically.

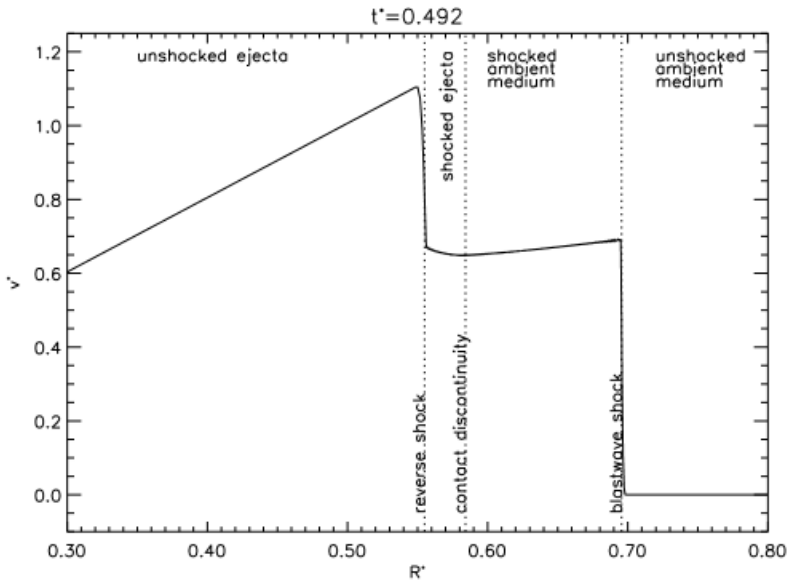

Figure 4.1: Simulated velocity-position distribution of a SNR in the Sedov-phase with uniformly dense CSM and uniform velocity distribution of ejecta. The selfsimilar scales are expressed in $t_{ch} = E^{-1/2} M_{ej}^{5/6} \rho_0^{-1/3}$ and $r_{ch} = M_{ej}^{1/3} \rho_0^{-1/3}$. With an ejecta mass of $3.0 M_\odot$, an explosion energy of 1 B the CSM density $\rho_0 = 1\text{cm}^-3$, this represents units of $t_{ch} = 1184$ yr, $r_{ch} = 4,95$ pc and $v_{ch} = 4094$ km/s.

[22] As an example to illustrate this, Rayleigh scattering also takes place in earth's athmosphere: During daytime, the blue light from the Sun is more widely distributed across the sky than red light due to its more pronounced scattering.

[23] Due to the large abundances of hydrogen in the universe, the Balmer lines from far away galaxies are often well visible; because of the expansion of the universe, their redshift can be used to estimate the distance of such galaxies.

Part II
Cassiopeia A

5 Geometry

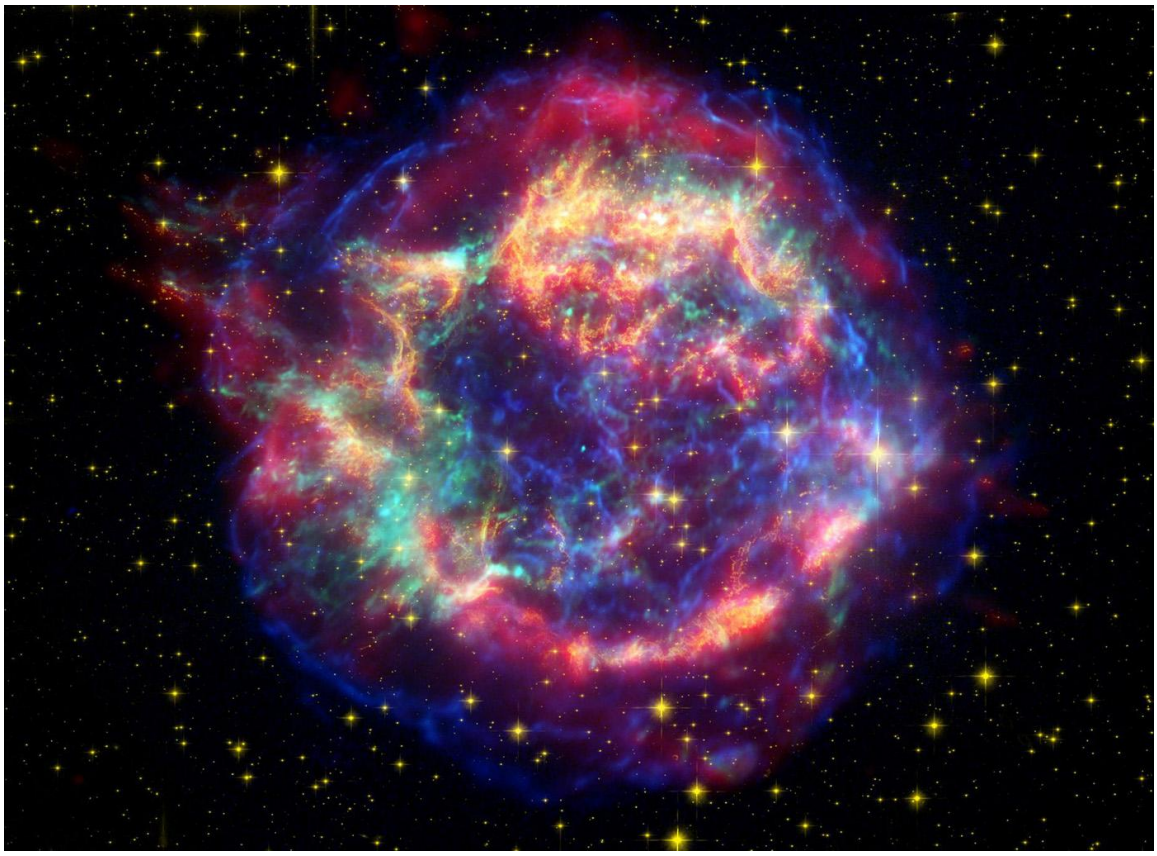

Figure 5.1: Multiband picture of Cas A (Source: NASA). Infrared 24 µm data from the Spitzer Space Telescope is shown in red, optical data from the Hubble Space Telescope in yellow and X-ray data from the Chandra X-ray Observatory in green (intermediate X-ray) and blue (broad-band X-ray). The precise observational bands were not defined by the source.

Cas A is highly asymmetric. As shown in Figure 5.1, the FS (the blue outer filaments) and the RS (bright multicolored ring) are clearly visible in the emitted spectra, so the SNR may be in the late free expansion phase or early Sedov-phase (see Chapter 3.3). The sharp turquois dot near the center of the SNR is a strong X-ray source which is believed to be the CCO. In the northeast[24] there is a clearly visible outflow of material, a so-called jet.
Especially in the RS, where high-energy turbulences occur, matter is distributed highly irregularily. The approximately circular FS and RS are not concentric, and the CCO is approximately colinear with those centers. The shocked ejecta appear to be bisected in the plane perpendicular to the connecting line, with a higher emittivity in the northwest and than in the southeast.
In this chapter, the basic structural geometry is elaborated to provide a foundation for further analysis without delving further into their origins. Unsophisticated models for some phenomena are however presented when appropriate.

[24] As the observing direction is inverted compared to maps of earths surface, so are east and west.

5.1 Distance and Age

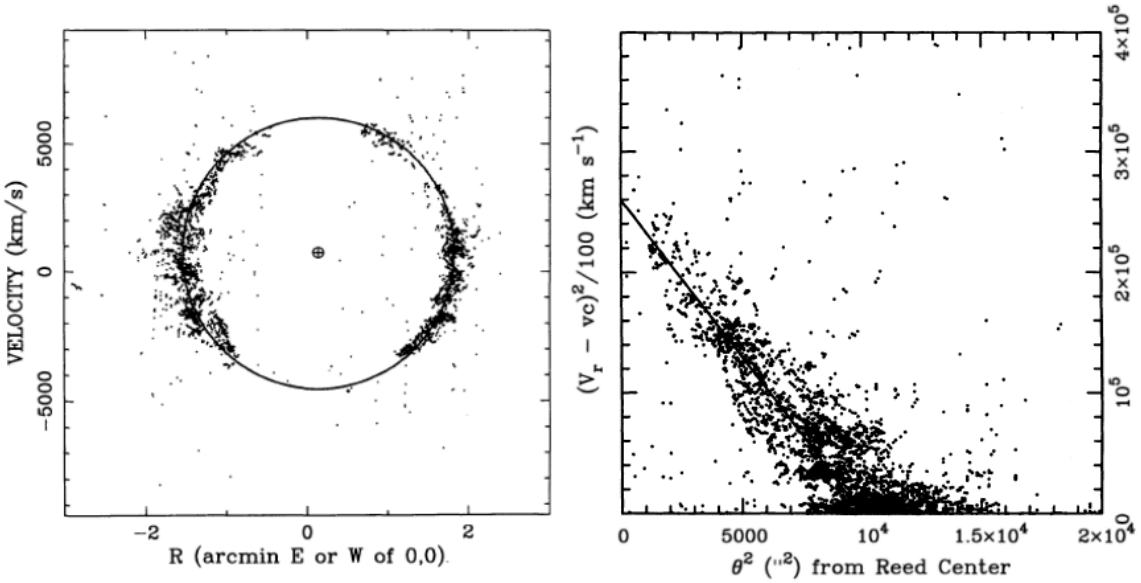

Figure 5.2: Approximation of distance-age ratio (Source: Reed et al. 1995). *Left:* Spherical fit of $D/\Delta T$. The position coordinate represents the distance from the assumed COE on the POS. *Right:* Same data presented on a linear plot.

The distance and age of Cas A are entangled in observation: The ratio of the actual and observed size of the object in the plane of the sky (POS) scales near-linearily (see Appendix A.1) with distance D, while the width along the line of sight (LOS) can be determined under the assumption of free expansion by Doppler-position mapping (see Chapter 4.2) with the free expansion time ΔT being the time since the explosion. The ratio $D/\Delta T$ as well as the position on the sky and the relative velocity of the center of expansion (COE) along the LOS are then fitted to a sphere.
While the unshocked ejecta would be the obvious candidate for this procedure as they fulfill the cirterium of free expansion to a high degree as described in Chapter 3.3, their irregular geometry (see Figure 5.1 or Chapter 5.5) does hardly allow spherical fitting. In front of the FS, a large number of fast-moving knots (FMKs) have been observed; even though technically being in a position where Doppler-position mapping is no longer applicable (see Chapter 4.2), they are not decelerated in the same manner as the shock front because the large voids between them only allow little accretion on the knots. Deviations from free expansion therefore are mainly caused by drag of the CSM, which is for now treated as being negligible.
Several different datasets of FMKs have been used to determine this ratio, while the often quoted analysis by Reed et al. (1995), recorded in the infrared/optical range ($1.6-2.0$ eV), is commonly accepted and will be used throughout this thesis. It results in $D/\Delta T_{1986} = 11.1$ pc/yr and the location of the COE at $23^h21^m10.8^s \pm 0.09$,+58°32‘32.0” $\pm$ 0.8 with a velocity away from the observer of 770 ± 40 km/s as shown in Figure 5.2 on the left.
The assumption of free expansion is supported by comparing these results to earlier observations; a deceleration of the FMKs would render the actual LOS velocity-position function sublinear, meaning that analysis of later-recorded data would lead to a lower $D/\Delta T$ ratio as the erroneously used linear velocity-position function would have to be compensated. However, analysis by Minkowski (1959) of 50 FMKs lead to the same ratio[25]. With this value, structures in the RS also form a sphere with high accuracy (see Chapter 5.4).

[25]Within both papers, the explosion date was assumed to be 1680, so the distance was calculated directly. However, there was little evidence at that time that this event actually was the SN of Cas A.

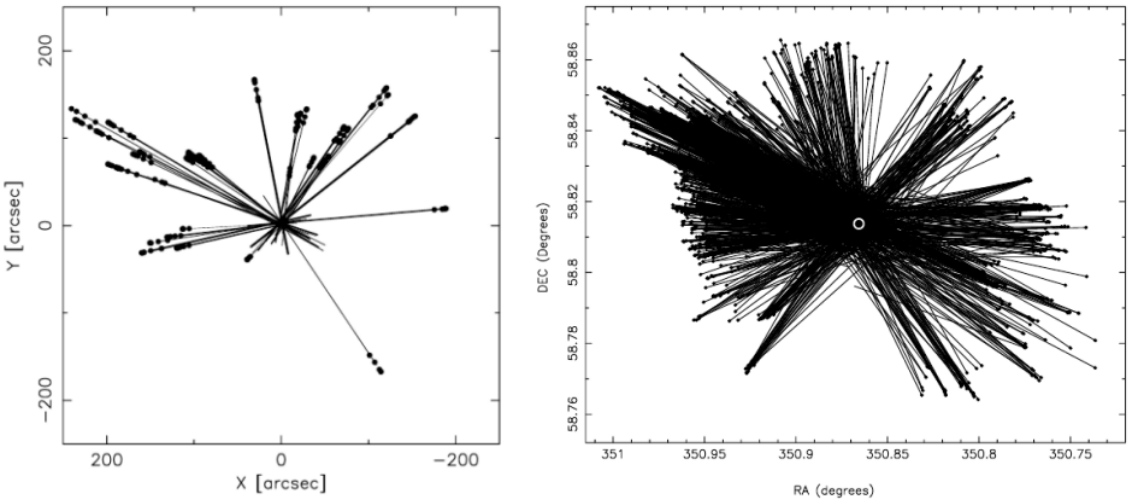

Figure 5.3: Approximation of age. *Left:* Linearily extrapolated motion from 1600 to 2004 of 17 bright FMKs observed for 48 years (Source: Thorstensen et al. 2001). *Right:* Linearily extrapolated motion from 1684 to 2004 of 1825 FMKs observed for 9 months (Source: Fesen et al. 2006a).

To estimate the explosion date of Cas A, the motion on the POS of a large number of FMKs over different timescales have been observed (17 FMKs over 48 years in Thorstensen et al. (2001), 1825 FMKs over 9 months in Fesen et al. (2006a)). Their proper motion was extrapolated linearily backwards in time as shown in Figure 5.3 and the expansion time as well as a COS fitted to the data; naturally, this is independent of the actual distance and the LOS velocity components. When using the data unfiltered, this results in an estimated explosion date around 1662 ± 27.
As they travel before the dense FS, radiative cooling is efficient for FMKs; to make them visible, heating, either by drag or absorption of the SNR emissions, is necessary. Because of this, small, dense FMKs are favorable for analysis as they are less decelerated by drag and have a reasonable cross section for reabsorbing their internal emissions. Using 72 hand-picked small, bright FMKs results in an estimated explosion date around 1671.8 ± 17.9.
As any remaining drag shifts this to a later date, this approximation coincides well with an observation by Flamsteed in August 1680, which is debated to be the SN of Cas A and will be used as the explosion date in this thesis. With the $D/\Delta T_{1986}$ computed earlier, the distance of Cas A is estimated to be $3.4^{+0.3}_{-0.1}$ kpc. Assuming the discrepancy of measured age and the Flamsteed observation is caused by drag results in a negligible difference in D (see Appendix A.2).
In Figure 5.3 on the right, the trajectories seem to match poorly with the COS. When filtering the dataset as described in the paragraph above, the intersections group significantly tighter (see Figure 5.3 on the left, with merely 17 FMKs remaining). Small, low-density knots cool quickly, so the filtered FMKs can be assumed to be large and possibly of high density. On these, the forces caused by drag and inhomogeneous[26] radiative heating from the SNR can cause disruption of the knots, leading to the observed divergence of trajectories.

[26] As the quantity of heat absorbed per area is dependent on the angle in which the area is facing the SNR, deformation caused by drag may lead to significant temperature gradients in the knot which may generate Rayleigh-Taylor instabilities.

5.2 Evolutionary Stage

As described in Chapter 3.3, the naive model of the FS is a comparably dense "wall" which is near-impermeable to the CSM and therefore loses kinetic energy by transferring momentum to the accreted CSM. Therefore, FMKs from the previous chapter do not represent the FS as their small size does not allow significant CSM accretion. The FS can be observed by the radiation caused by the heating due to the continuous collision.
Such emissions have been observed by Gotthelf et al. (2001) in the 4-6 keV range as thin circle line as shown in Figure 5.4 on the top left. In the same figure on the right, a circular fit was used to plot the intensity as a function of distance from the center of the FS. Narrow peaks can be seen in the radio and X-ray spectrum at a radius of roughly 153″ or 2.5 pc. Furthermore, there is a jump in the average polarisation angle of the recorded synchrotron radiation, indicating (without quantitative analysis) that there is a significant change in ambient conditions which reflects in a different magnetic field.
While there are no general line emission features in the presumed FS, colocated clumps with strong 1.86 keV Si transistion lines are seen in the north and south of the remnant as shown in Figure 5.4 on the bottom left. However, as these lines do not exhibit the same peak as the radio and X-ray spectra and jets spread far beyond the borders of the FS, the expansion rate of the FS cannot be extrapolated from the observed doppler shift in those lines.

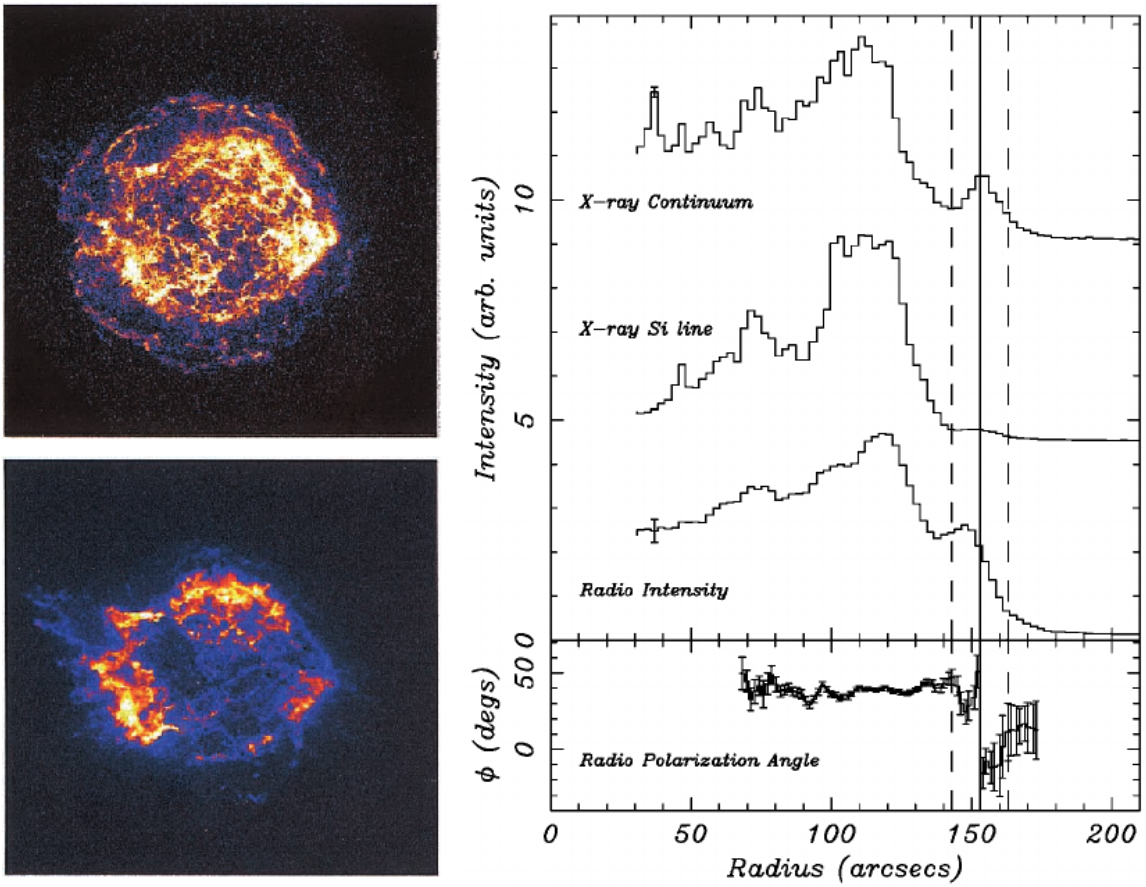

Figure 5.4: Location and properties of the forward shock (Source: Gotthelf et al. 2001). *Top Left:* 4-6 keV emissions over entire remnant. A perforated thin line can be seen to form a rough circle around the remnant. *Bottom Left:* 1.86 keV Si transistions over entire remnant. In the north and south, seperated clumps appear close to the presumed FS. *Right:* Intensity of various emission bands as well as synchrotron polarisation angle plotted as a function of the distance from the center of the presumed FS marked by the line.

In contrast to the FS, the RS sweeps inward (relative to the FS) though the ejecta, wherefore its motion cannot be characterized by the observed velocity of knots. As the shock heating produces an "afterglow" and the RS moves at sonic speed relative to the (freely expanding) unshocked ejecta, it is reasonable to neglect radiative heating of unshocked ejecta by the RS and use the inside radius of the emissive plateau as its position.
In Figure 5.1, such a shock heated plateau can be clearly seen in yellow and green, known as the "bright ring" (BR) and is of substantial width, indicating weak radiative cooling due to high density. Ignoring its diffuse and asymmetric structure, the RS position can be estimated by fitting a circle to a high gradient in emittivity, which results in a radius of 95" or 1.6 pc as shown in Figure 5.5 when done in the radio and X-ray band, about two thirds of the forward shock's radius.
Furthermore, its COE is offset to the northwest by 13" or 0.22 pc relatively to the FS center. In a naive model, the plateau of shocked ejecta being apparently brighter in the northwest than in the southeast is coherent with the COE offset when assuming that the angular distribution of the ejecta mass relative to the RS and FS COEs is approximately uniform as the smaller distance between FS and RS implies higher density and thereby less efficient radiative cooling, resulting in a more pronounced "afterglow".

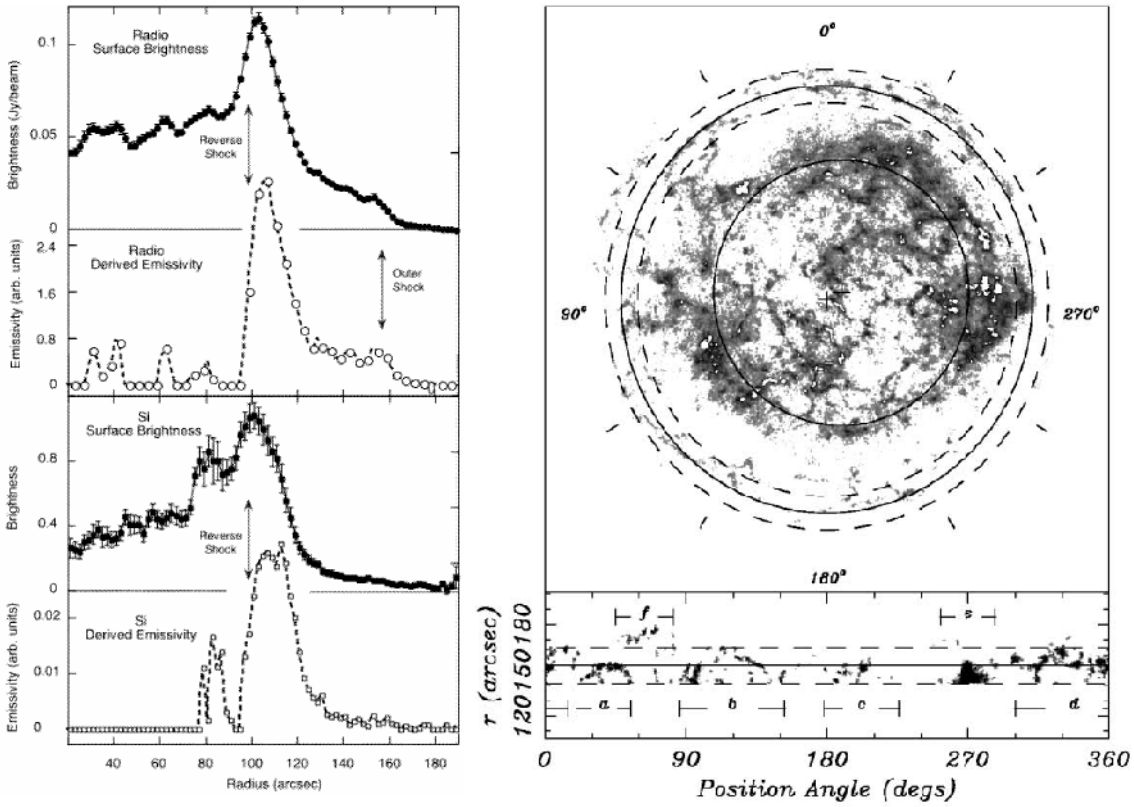

Figure 5.5: Location of the reverse shock (Source: Gotthelf et al. 2001). *Left:* Emittivity profiles in the radio- and X-ray band as a function of the distance of the presumed RS. A high positive gradient is centered at around 95". The FS peak is barely visible because it is not concentric with the RS. *Right:* Center offset of circular FS and RS fit. The diffuse structure and asymmetry of the reverse shock is clearly visible. Below, the segments of the FS are displayed and labeled. Segment f has been excluded from the fit since a jet is in its proximity (see Figure 5.1), explaining its higher distance from the COE. Segment e has been excluded because it is not clearly segregated from the inner ejecta.

To assess the expansion speed of the FS, 29 clumps have been tracked over two years, resulting in an average expansion speed of 5.0×10^6 m/s (DeLaney and Rudnick 2003) as shown in Figure 5.6 on the left. Using a simple deceleration model with the remnant's radius $R_{FS} \propto \Delta T^m$, where $m = 1$ represents free expansion, the observation suggests $m \approx 0.7$. While the exact value is meaningless as this model hardly represents the mechanisms of SNR evolution, it shows clearly that the FS has decelerated significantly and the remnant has entered the Sedov-phase[27].
Multiple studies of the RS's expansion speed have been conducted in the radio, optical and X-ray band, yielding drastically different results ranging from 1.2×10^6 m/s to 5.3×10^6 m/s depending on the observed energy band (DeLaney and Rudnick 2003, and references therein). A common factor of most of these studies however was their choice of observing small-scale emittivity gradients; considering the possibility of "gaps" in the ejecta, it is probable that instead of the RS, the afterglow of individual clumps had been measured. This suspicion is supported by doppler measurements of similar emittivity gradient peaks in the LOS; particularily in the X-ray, the supposed RS expansion on the POS was 40% faster than the associated Doppler speed of the clumps. Because the reverse shock moves backwards through the material by definition and doppler shifts show the emitting material's velocity, it is clear that these small-scale measurements do not represent the RS, but rather the movement of the material itself.
A radio large-scale observation of synchrotron emissions in the south of the remnant produces an expansion rate of 1.2×10^6 m/s, significantly slower than the slowest small-scale result of 1.8×10^6 m/s. Within this thesis, the large-scale expansion speed will be accepted as the RS expansion speed[28]. Fitting the RS and FS diameter ratio to the evolution model of Truelove and McKee (1999) shows excellent conformity with this result, producing a FS and RS speed within the uncertainity as indicated in Figure 5.6, confirming that Cas A is in the early Sedov-phase.

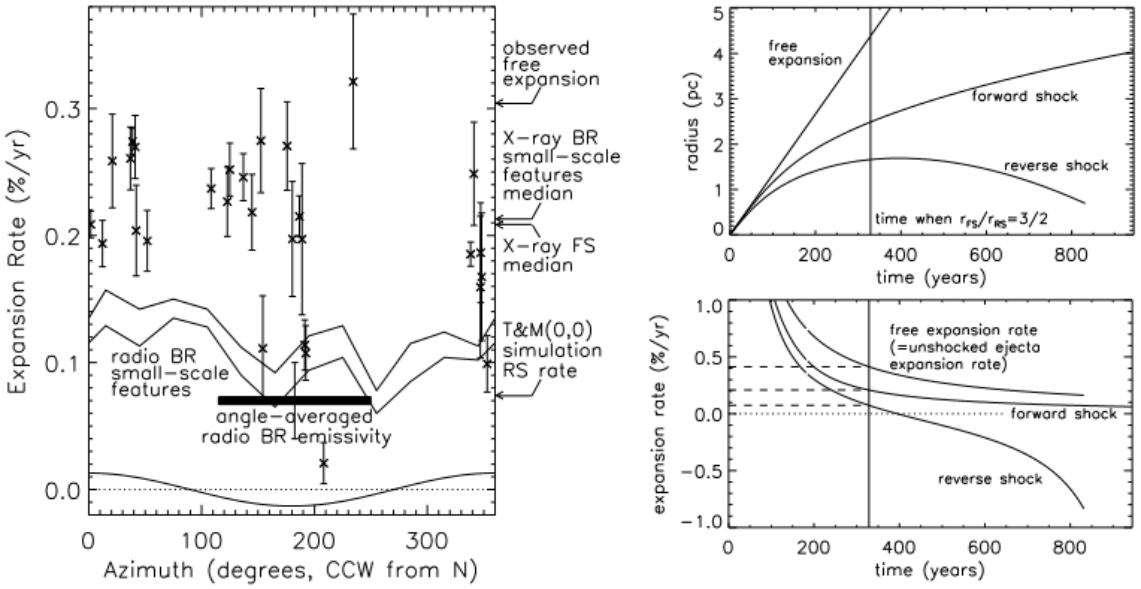

Figure 5.6: Expansion of forward and reverse shock (Source: DeLaney and Rudnick 2003). *Left:* Relative expansion of FMKs, FS and the BR with the two solid lines representing the error band of the small-scale movement. The thick line represents the average large-scale RS emittivity gradient movement, its length represents the angle covered in the analysis. *Right:* Different depictions of the same model by Truelove and McKee (1999). The originally dimensionless model has been fitted to the ratio of FS and RS diameter age of Cas A.

[27]From a theoretical standpoint, one could argue that the existence of a pronounced reverse shock already confirmes that the remnant is in the Sedov-phase; however, there is little empirical evidence to support that general claim.

[28]Assuming free expansion, the outermost unshocked ejecta move at 5×10^6 m/s, resulting in a collision speed and thereby speed of sound of 3.8×10^6.

5.3 Compact Central Object

A pointlike X-Ray source near the center in Cas A is shifted to the southeast by 7" or 0.1 pc relative to the FS center in the exact opposite direction as the RS (Gotthelf et al. 2001). It has been recorded in the near-infrared, optical and X-ray spectrum without finding significant line features. The high ratio of X-ray to optical flux $\sim 10^4$ (Fesen et al. 2006b) is not agreeable with it being a star[29] behind Cas A; furthermore, the spectrum does not match the characteristical emissions of active galaxy nuclei, suggesting that it indeed is the remainder of Cas A's progenitor's core (Pavlov and Luna 2009).
Typically, a Type II SN is believed to collapse into a black hole or a neutron star, the former emitting X-rays predominately from the heating of the ambient matter it accretes, so strong recombination lines should be visible. This is not the case; also, the X-ray emissions are too strong to be explained by such a process, and no fluctuations in brightness have been observed as would be usual for an accreting object. Because of the absence of line features in the spectrum, it is not possible to observe any doppler movement. Observations of the POS movement have not yet yielded statistically significant results.
A simple blackbody model, which would be a decent approximation for a rotation-free NS, with the observed[30] radius $R^\infty \approx 0.9$ km results in $T^\infty \approx 4 \times 10^6$ K and poorly fits at energies above ~ 4 keV as shown in Figure 5.7. As both values are highly atypical for a NS, usually being in the magnitudes of 10 km and 6×10^5 K, a rotation-free NS can be ruled out.
Above a period of 0.68 s, no pulsations were found[31]. While many pulsars have periods in the millisecond range, virtually all of them are accompanied by pulsar wind nebulae from early on and show a hard power law spectrum. As there is no sign of the former in the radial profile and the spectrum is soft, it is improbable that Cas A's CCO is a regular pulsar. Comparing the spectrum with more exotic NS types, Pavlov and Luna (2009) suspect that the CCO might be an anti-magnetar, although the luminosity exceeds the typical range of known examples of this NS type.

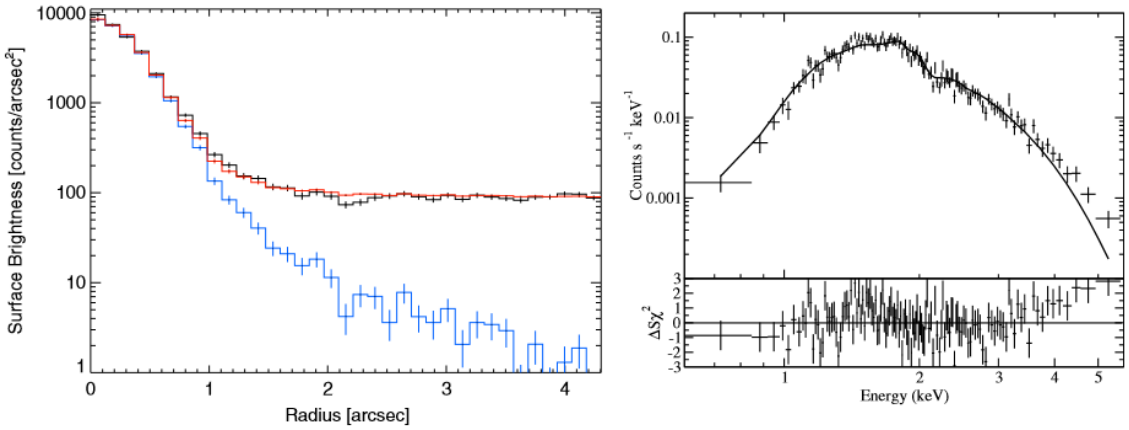

Figure 5.7: Observations of Cas A's presumed CCO (Source: Pavlov and Luna 2009). *Left:* Radial profile of Cas A's CCO (black), simulated point source emission (blue) and the same with added simulated backgound (red). *Right:* Observed CCO X-ray emissions filtered by an extinction model and fitted blackbody model with residuals plotted below.

[29] The spectrum from a star would be approximately blackbody radiation filtered by the frequency-dependent extinction parameters of the ISM; with an estimated extinction in the optical band of $A_V \approx 6$, this would require a distance greater than agreeable with the observed brightness.

[30] As the relativistic effects on the surface of a NS can be substantial due to its high density, the actual parameters need to be compensated by accounting for gravitational reddening, i.e. $R = R^\infty g_r$ and $T = T^\infty / g_r$ with the gravitational redshift parameter $g_r = \sqrt{1 - 2GM/Rc^2}$.

[31] For this, the signal exposure time is 0.3 s, so Shannon-Nyquist downsampling is heavily dampened and does not provide significant extension of the observational range.

5.4 Structure of the Shocked Plateau

The shocked ejecta that recently passed the RS are an excellent candidate for 3D analysis because their high electron density supports recombination and along with the high thermal energy produces strong line features in the infrared and X-ray. By consulting Figure 4.1, which, albeit displaying a slightly later stage in the SNR evolution, predicts severe deceleration upon RS encounter, it becomes clear that a free expansion approximation is not applicable; also, the X-ray movement measurements by DeLaney and Rudnick (2003) show significant deceleration with $m = 0.5$ for LOS movement[32], a factor comparable to the results of the model by Truelove and McKee (1999).

However, the model also predicts that there are no shocked ejecta moving at velocities close to free expansion, yet such ejecta exist in large abundances in Cas A as will be shown in the following. This contradiction indubitably is caused by the onedimensional model and can be resolved by assuming a "porous" ejecta structure, similar to the FMKs. In absence of a sufficiently detailed model, in order to get an insight into Cas A's three-dimensional structure, each group of ejecta is to be treated individually and tested for consistency.

As shown in Figure 5.8 and anticipated in Chapter 5.2, the deceleration appears to be dependent on the energy domain: A spherical fit of infrared [ArII] emissions produces an expansion factor of $m = 0.89$, while the X-ray Fe-K lines form a sphere segment in the back of the remnant (relative to the observer) when a modified POS X-ray BR expansion rate ($m = 0.61$) from Koralesky et al. (1998) (originally $m = 0.66$) is used (DeLaney et al. 2010).

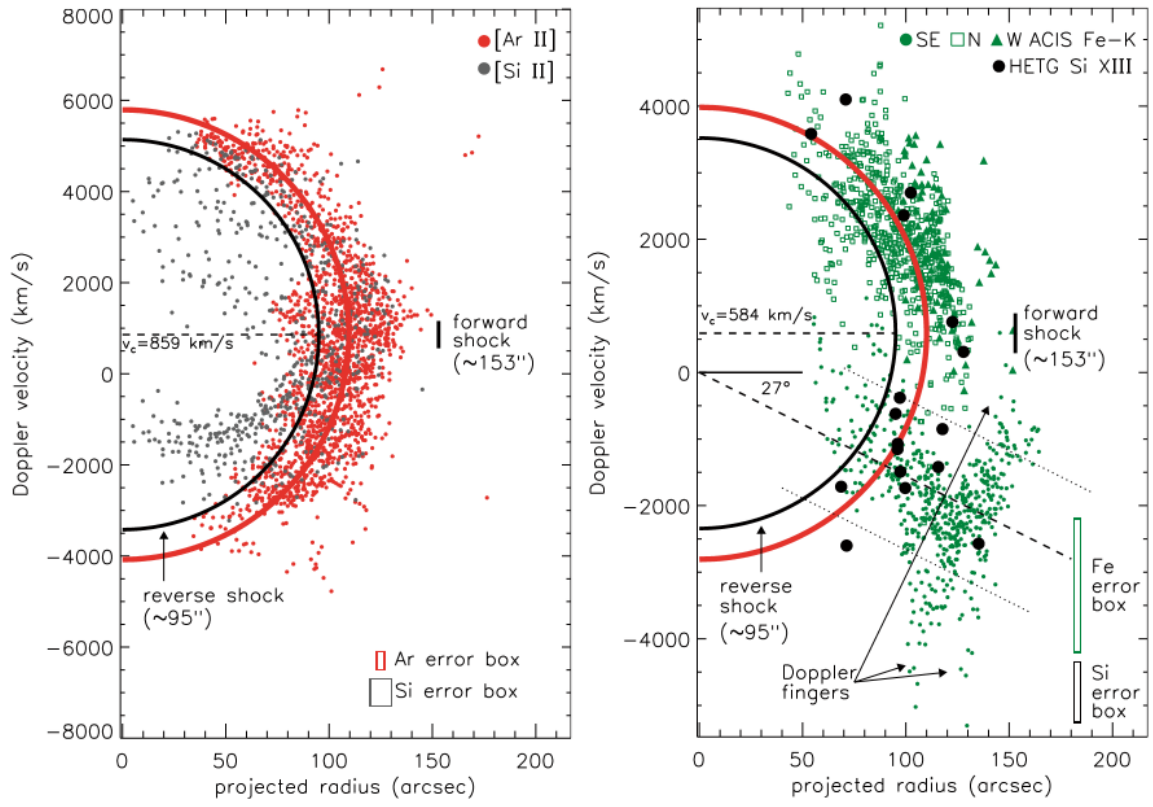

Figure 5.8: Energy dependency of velocity-position function in the shocked plateau (Source: DeLaney et al. 2010). *Left:* Infrared [ArII] (6.99 µm) and [SiII] (34.82 µm) emission lines with a spherical fit of the former. *Right:* X-ray [SiXIII] (1.865 keV) and Fe-K (6.6 keV) plotted with a velocity-position functiond derived from X-ray RS observations in Koralesky et al. (1998).

[32] According again to the power law model $R \propto \Delta T^m$, which in this case has no connection with reality as the shocked ejecta have been in free expansion before passing the RS; however, it is useful for comparing deviations from free expansion in a naive manner.

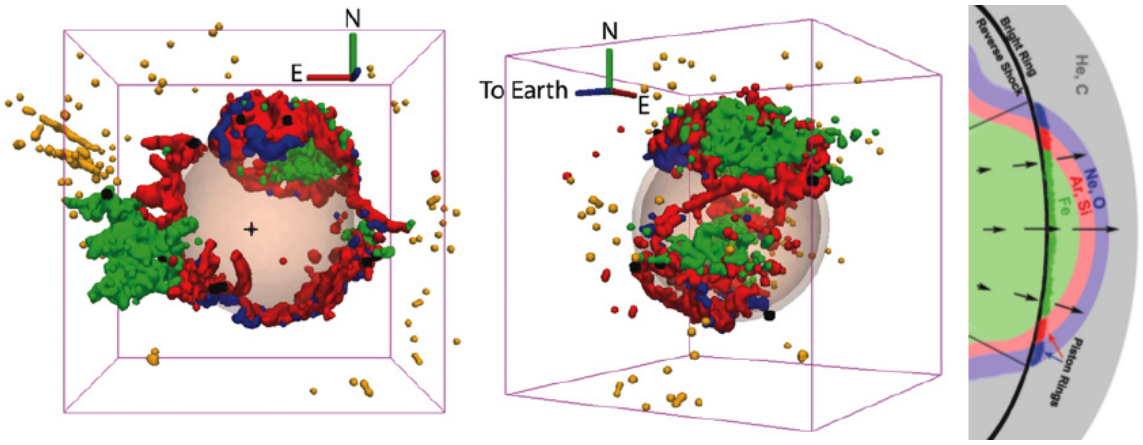

Figure 5.9: 3D map of the shocked plateau (Source: DeLaney et al. 2010). *Left and Middle:* Composite maps with [ArII] emissions (red), regions of high [NeII]/[ArII] emisson ratio (blue), Fe-K emissons (green), [SiXIII] (black) and optical FMKs (yellow). *Right:* Cartoon of the piston model.

The Fe-K emissions show irregular structures in the southeast as shown in Figure 5.8 and marked as "Doppler Fingers", which extend close to the LOS; this implies that they are not actual geometric structures, but radiate at a different wavelength in their rest frame due to a different ionisation state, caused by a locally different temperature. As there are no 3D temperature maps of Cas A, they have been shifted groupwise between the dotted lines to roughly compensate this effect.
This is justified by the jet-like iron outflow in the southeast of the remnant: As in the north and southwest, an accumulation of iron is surrounded by an argon ring as well as neon ring segments. This can be explained by piston-like asymmetric expansion of the ejecta as shown in the cartoon on the right of Figure 5.9, where differences in radial velocities can cause Rayleigh-Taylor instabilities and thereby heat up. This theory is reinforced by the [SiXIII] emissions found near the edges of the pistons which require a higher temperature than the generally present [SiII] lines. The inner part of the piston meanwhile is less subjected to reverse shock compression, resulting in a comparably lower temperature. The pistons in the north and southwest are less pronounced than the one in the southeast, so little to no visible "Doppler fingers" are produced.
This piston model also accounts for the observed difference in observed LOS ($m = 0.47$ from Willingale et al. (2002)) and POS expansion speed: Ejecta at the edge of the pistons can be assumed to be diverted into the pistons' directions, concentrating the ejectas trajectories. As the pistons are aligned close to the POS, ejecta with initially high doppler velocties are diverted to move rather along the POS than the LOS. This results in a spatially variable distortion of the velocity-position function; as this requires extensive modelling, the earlier use of an expansion rate in-between the POS and LOS expansion rate justified to be a reasonable compromise. For the infrared argon, neon and silicon emissions, as their pistons have cooled down and are no longer visible, the effect is inverted, hinting at why the LOS expansion speed in the optical exceeds the POS expansion speed by 9%.
The order of ejecta layers in the shocked plateau matches the nucleofusion layers in the core as described in Chapter 2.2; the silicon ejecta that appear to lie inside of the iron layer in Figure 5.8 actually fill up the "holes" in Figure 5.9 and can be approximated well as two disks as shown in Figure 5.10. As of yet, there is no evidence of any significant occurences of heavier elements outside of these disks; presumably, there was no layer overturn, but the explosion was oblate and the layers of heavier elements are yet to reach the reverse shock in that region. The pistons align on a similar plane and form a tripole, with the strong southeast piston being countered by the two weaker north and southwest pistons. Its axis aligns well with the offset of FS, RS and CCO, so there is an apparent large-scale symmetry plane in Cas A.

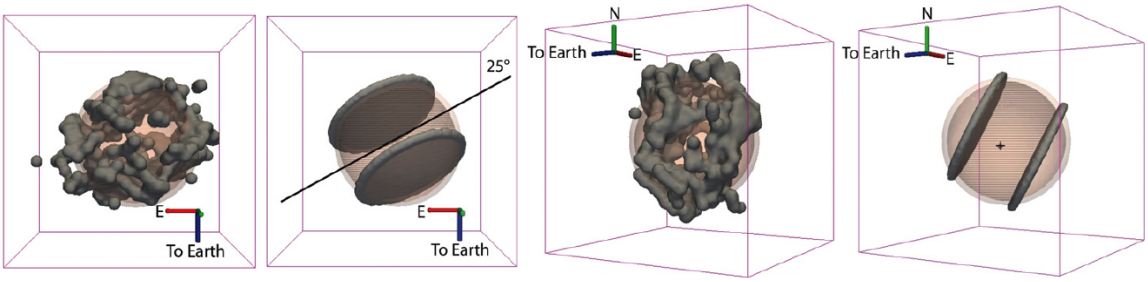

Figure 5.10: 3D map of [SiII] emissions in proximity of the bright ring and large-scale planar symmetry approximation (Source: DeLaney et al. 2010).

5.5 Interior Structure

As the unshocked ejecta were not yet heated by the reverse shock, they are comparably cold and do not radiate substantially in high energy domains. An extensive search for emission lines in the infrared (5-38 µm) was conducted (Smith et al. 2009; Isensee et al. 2010) with high spectral and spatial resolution over the entire remnant and revealed strong sulfur and silicon line emissions as well as emissions around ~ 26 µm, which could fit either [FeII] or [OIV] lines.
While the near-absence of 17.94 µm [FeII] emissions in the interior of the BR hints at their identity, a spatial comparison with the silicon clumps show excellent conformity when identifying them as oxygen; as the wavelenghts differ by $\sim 0.4\%$, identification as iron would shift them about 10^6 m/s or, assuming free expansion, 0.4 pc towards the observer, implying in a layer overturn on the front of the remnant, but not on the back as shown in Figure 5.11 on the left, so it is highly likely that the majority of those emissions are indeed oxygen lines. Infrared neon and argon lines, while being observable in the shocked plateau (not depicted), are hardly present in the interior and the thick disks. However, as the emittivity is very sensible to the density (see Chapter 4.1), this does not imply absence of those elements.
The spatial distribution of silicon and sulfur appears to be nearly identical as shown in Figure 5.11 on the right, which comes as no surprise since the isotopes are neighbors on the bidirectional α-ladder (see Chapter 2.2.4). They also show an excerpt of the tilted disks in Figure 5.10: The higher resolution reveals the disks on the back as well as the interior filaments to be less than 7×10^4 m/s thick in the velocity space. The disk towards the observer on the other hand, described as interwoven filaments by Isensee et al. (2010), exhibits a width of 1.5×10^6 m/s; for free expansion, this represents 0.5 pc in comparison to 0.02 pc of the disk on the back.
Near-infrared [SiII] 907 nm and 953 nm observations over a larger part of the remnant, including parts of the BR, show rings in the interior that do not align with the pistons found in the shocked plateau as shown in Figure 5.12. While oxygen is mostly colocated with silicon and sulfur in the thick disks, it seems to complement some of the arc-like silicon/sulfur structures found in-between the disks when comparing the left and middle plots in Figure 5.11, so it is reasonable to assume that more rings might become apparent when expanding the data showed in Figure 5.12 with large-area oxygen observations.
It is suspected that the radiative pressure from radioactive ^{56}Ni plumes in the early post-SN phase might have caused low-density bubbles in the expanding debris and thereby caused thin high-density features (Milisavljevic and Fesen 2015). Comparison of the FMK distribution in Figure 5.3 to the piston geometry in Figure 5.9 shows no apparent common axis, suggesting that high-order multipoles have rearranged the symmetric properties in-between, supporting the radiative plume model. It is however questionable whether the abundances of the X-ray active iron in the shocked plateau suffice (as ^{56}Fe is the stable daughter nucleus of ^{56}Ni) to have such an impact on the early explosion, strongly recommending quantitative elemental analysis in order to proceed with exploring the history of Cas A.

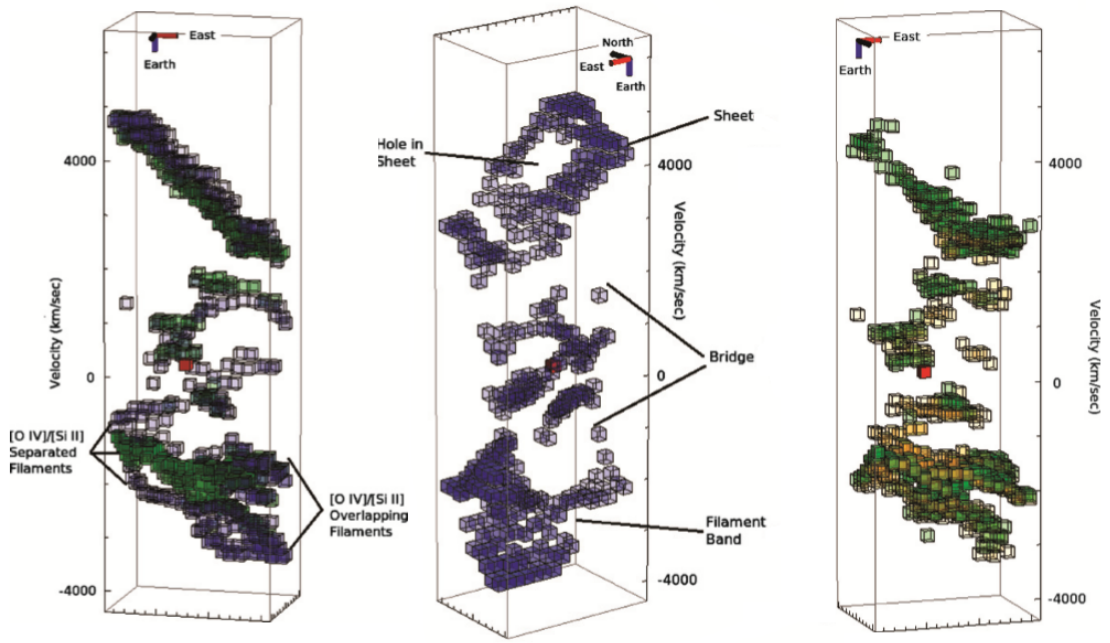

Figure 5.11: Distribution of elements in the unshocked ejecta within a $54'' \times 40''$ (0.89×0.66 pc^2) rectangle close to the COS with the velocity axis stretched by a factor of 1.8 to provide better visibility of interior features (Source: Isensee et al. 2010). *Left:* Alignment of [OIV] (blue) and 34.81 µm [SiII] (green) lines. *Middle:* Structure of [OIV] lines. *Right:* Superimposed [SiII] (green) and [SiIII] (yellow) lines.

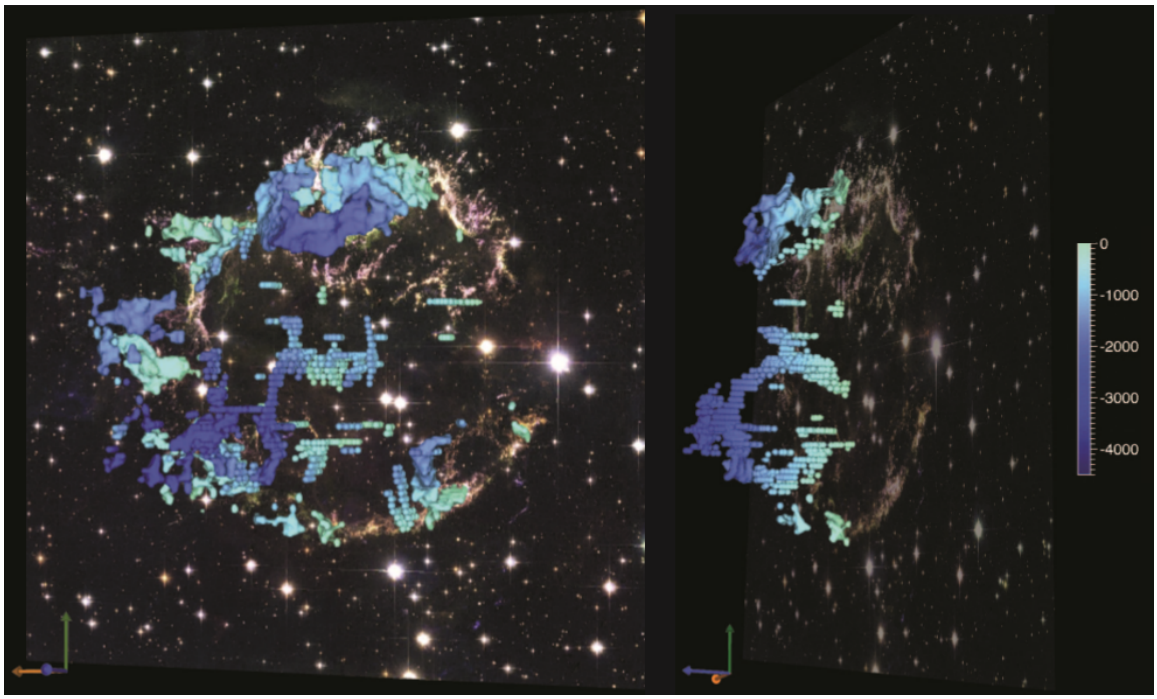

Figure 5.12: Structure of the unshocked near-infrared [SiII] ejecta. For better visibility, only blueshifted lines are displayed; similar rings not relatable to observed RS pistons are found in the redshifted ejecta. The velocity scale is given in km/s (Source: Milisavljevic and Fesen 2015).

6 Timeline

While the geometric structure has revealed many properties of Cas A, the fundamental question about the SN type is yet unanswered. While traces of weak hydrogen lines have been found in the fastest FMKs of Cas A with velocities of about 10^7 m/s, their low intensity leaves the possibility that they merely are accreted and collision-heated CSM. Furthermore, the apparent presence of multiple symmetries, particularly the FMK dipole and the large piston tripole, suggest dominance of different asymmetric processes at different evolutionary stages. To tackle these questions, more information about the early life of the remnant is required.

6.1 Supernova Type

In 2007, a sudden emittivity jump was observed in a circular area in a cloud residing at a POS distance of about $80'$ in the northwest of Cas A (Krause et al. 2008). The differential infrared spectrum in Figure 6.1 shows characteristical P-Cygni absorptions: Blueshifted relative to the doppler-widened peaks of the transistion lines, there are pronounced notches in the continuous spectrum. In the general case, these are caused by line absorption in rapidly expanding material shells around stellar objects in their broadband (e.g. blackbody) spectra. The total width of the hydrogen line amounts to 1.7×10^7 m/s and the P-Cygni notch centers at 1.1×10^7 m/s, leaving little doubt with identifying the emissions with a SNR early after the explosion.
If this was a direct observation of a galactic SN, it would exhibit considerably higher brightness; an extragalatic SN of sufficient distance on the other hand would be subjected to significant redshift due to the expansion of the universe, which is not visibile in the spectrum. Because of this, it is clear that the observations show a light echo (LE); as such, the flux is fairly high, so the reflecting cloud as well as the SNR are required to be in close proximity, confirming that this is indeed Cas A's LE. From the POS distance and the increased length of the light path as given by the presumed explosion date, the cloud is known to reside at about 19 pc behind Cas A's central POS, resulting in a scattering angle of 104°.
The spectrum in Figure 6.1 is compensated with respective angular scattering cross sections. Since the infalling angle is nearly perpendicular to the LOS, cloud width deconvolution is not necessary. While the presence of hydrogen lines confirmes that Cas A emerged from a Type II SN, comparison with the early spectrum of Type IIb SN1993J (both individually dereddened) shows striking similarity[33], pressing that Cas A's progenitor erupted in a Type IIb SN.

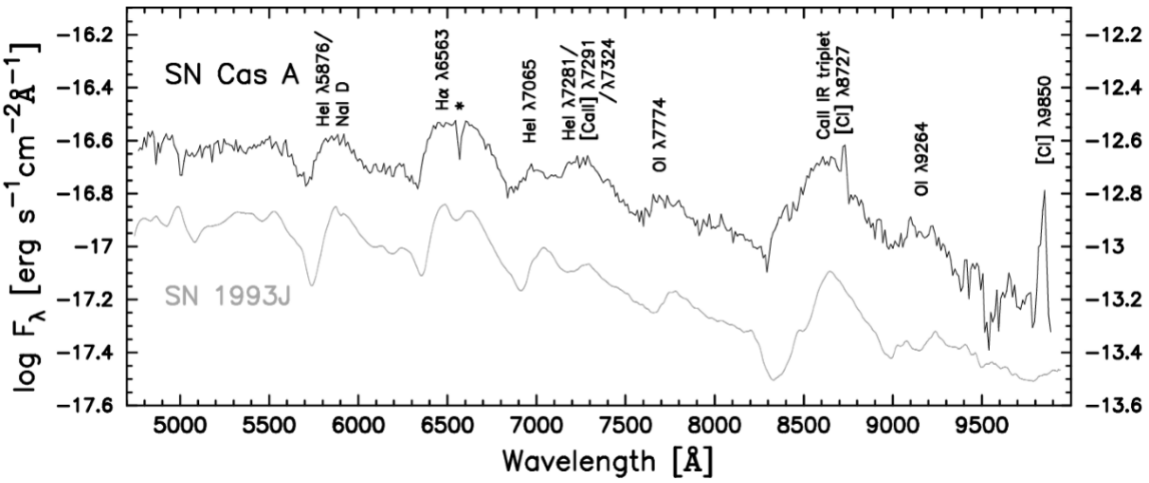

Figure 6.1: Compensated spectrum of a LE reflecting the early SNR in comparison with the spectrum (shifted by $\log F_\gamma = -4$) of the Type IIb SN1993 (Source: Krause et al. 2008).

[33]Typically being weak in a SN spectrum, the carbon lines in Cas A's LE spectrum probably do not originate from the SNR itself, but from carbon in the reflecting cloud excited by the SNR's blackbody radiation.

Three other LEs similarily attributable to Cas A have been observed and compared to the infrared spectra of various Type Ib, Ic, IIb and II-P SNe (see Figure 4 in Rest et al. 2011), with the result that the very similar confirmed IIb spectra are the best fit by far for Cas A's LEs.
Moreover, these LEs provided insight in Cas A's early spectrum from different observational perspectives. Most major differences can be traced back to the uncertainity in estimating the reddening and cloud width deconvolution parameters, the Hα and [HeI] emissions display a higher blueshift in their absorption notches from one particular LE, 3×10^6 m/s and 4×10^6 m/s respectively faster than their equivalents in other LEs as well as the absorptions observed in SN1993J as shown in Figure 6.2 on the left. The Hα notch converges towards the high hydrogen shell expansion speed of the equally Type IIb SN2003bg.
Comparing the respective perspectives with the shocked plateau data from Chapter 5.4 as in Figure 6.2 on the right shows that the higher expansion speed observed in the LE goes through the edge of one of the large pistons. Notably the velocity ratio of 30-40% matches well with the difference in proper motion and doppler X-ray clump expansion speed in the reverse shock as described in Chapter 5.2, supporting the author's notion of diversion induced by Rayleigh-Taylor instabilities at the pistons' edges described in Chapter 5.4.
The differential images were recorded from two observations with a time difference of three months (2521), one year (2116) and two years (3923) (Rest et al. 2011). The exact point of the recorded Cas A spectrum after the explosion is not precisely known, but below these intervals. Since the hydrogen and helium shells form the outermost layers of the progenitor and the CSM's density is reduced in close proximity to the star due to its radiation pressure, it is not likely that the observed velocity differences are caused by rapid deceleration. Since the perspective of the high-velocity region does not align significantly better with the FMK jets shown in Figure 5.3 than the others, it is likely that the piston structures developed during the explosion.

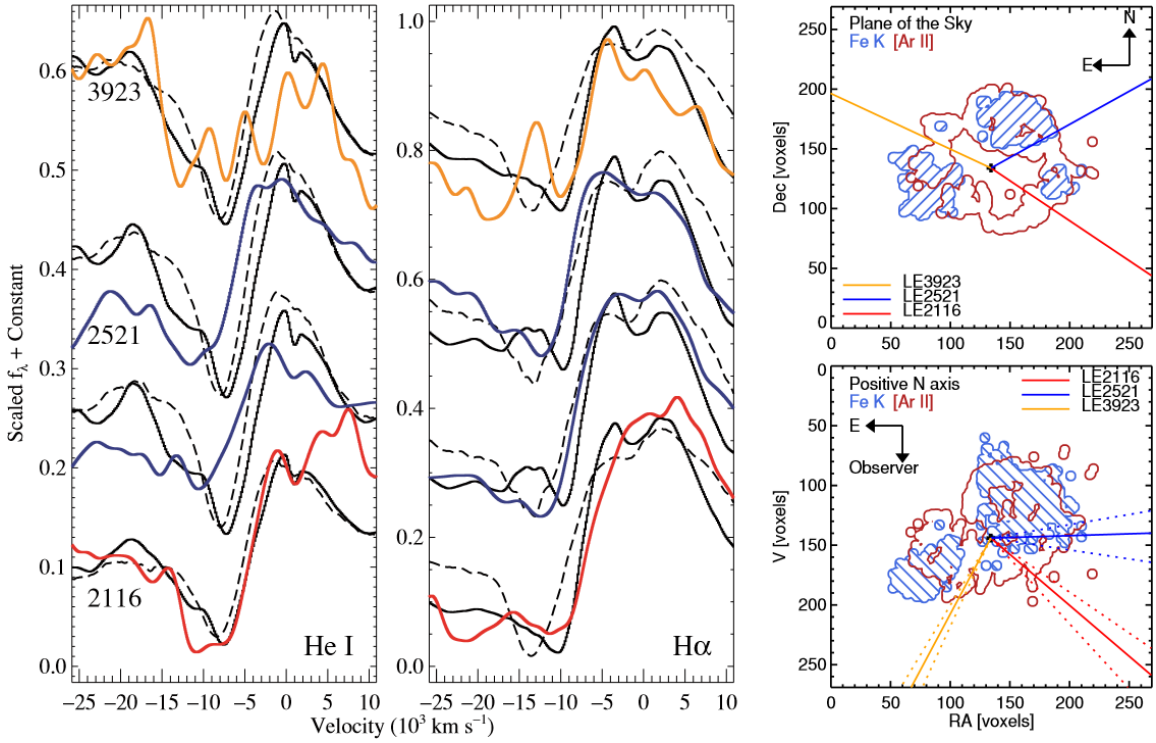

Figure 6.2: LEs from different perspectives (Source: Rest et al. 2011). *Left:* Spectrum of [HeI] and Hα lines with wavelenghts converted to doppler velocities from different LEs. The blue and violet line represent the same LE recorded with different instruments. *Right:* Presumed directions of LE clouds calculated with the necessary elongation of the light path superimposed with shocked plateau data from DeLaney et al. (2010).

6.2 Progenitor Mass

The SN type implies a progenitor mass of $25 - 40 M_{\odot}$ as shown in Table 3.1. As radioactive decay rates are strictly nuclear processes and as such hardly affected by ambient conditions, abundances of strong γ-sources can be determined with high precision; this, along with the expected ejecta ratios described in Chapter 3.3.1, can help narrowing the presumed progenitor mass range.

Because of the long decay lifetime of ^{44}Ti, the flux is still sufficiently strong to derive its inital abundance in the ejecta with high precision. Its daugther nucleus ^{44}Sc decays comparably fast as shown in Figure 6.3 on the left, meaning that the observations of both decays should result in very similar count rates of the 67.9 keV and 1157 keV deexcitation emissions; furthermore, as the produced ^{44}Sc* requires two deexcitation steps most of the time, the 78.4 keV/67.9 keV ratio is expected to be near 99% (Bleeker et al. 2002).

These predictions do not mirror the observations[34]: As reported in Siegert et al. (2015) and shown in Figure 6.3 on the right, the ^{44}Ca* deexcitation flux is significantly higher than the one of ^{44}Sc*. As ^{44}Sc's only source is ^{44}Ti decay and neither interstellar exctinction nor electromagnetic diversion can play a significant role in this energy regime, this appears paradoxical and can, apart from suspecting an observational or analytical error which is unlikely given the multitude of measurements, only be resolved by assuming that there is a process capable of reexciting the calcium nuclei. Collisions with CRs accelerated in Cas A's diffuse shock might be the cause; in this case, since the mass of calcium nuclei increases over time, the additional radiation should do so as well; given the error bars in Figure 6.3, this might however take decades to be statistically significant.

Either way, the 1157 keV line does not represent the ejected ^{44}Ti mass. Both ^{44}Sc* deexcitation line fluxes match well; as the scandium nuclei decay rapidly and the cross section implied by the additional calcium emissions should not affect them significantly, their resulting initially ejected ^{44}Ti mass of $(1.37 \pm 0.19) M_{\odot}$ can be assumed to represent Cas A well, significantly more than predicted in Figure 3.2. Notably, only traces of titanium are found in the pistons, while the bulk appears to reside in the interior (see Figure 3 in Grefenstette et al. 2014), disagreeing with the naive shell order derived from the nucleogenesis processes.

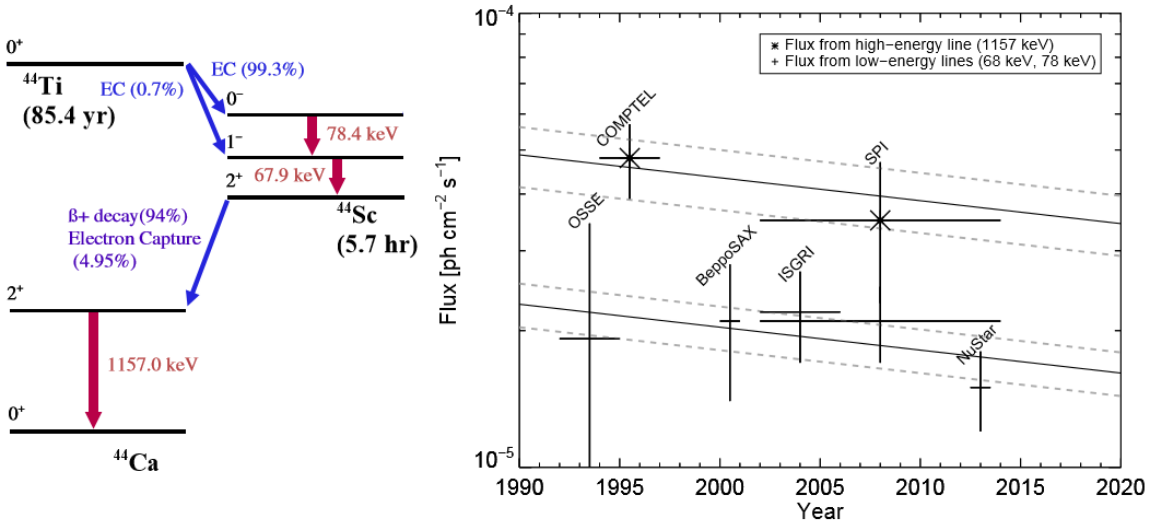

Figure 6.3: Identification of the initially ejected ^{44}Ti mass. *Left:* Decay scheme of ^{44}Ti (Source: Bleeker et al. 2002). *Right:* Results of a variety of studies regarding ^{44}Ti decay flux, sorted by the relevant nuclei. The solid lines represent mean values fitted the natural decrease in flux, the dotted lines indicate the statistical error (Source: Siegert et al. 2015, and references therein).

[34] As a historical sidenote, Cas A was the first SN in which ^{44}Ti was observed.

Because of the comparably short mean decay lifetimes of ^{56}Ni and its daughter nucleus ^{56}Co of ∼9 days and ∼111 days respectively (the next step in the decay chain being the stable product ^{56}Fe) and the time since the SN being $\sim 10^{10}$s, virtually no radioactive isotopes are left to observe. During the early phase of the SN however, because of the very same properties, the nickel ejecta deposit their available nuclear energy at a high rate into heating of the expanding plasma. Based on this, Eriksen et al. (2009) estimated an upper limit for the radioactive nickel mass as described in the following:
For virtually all SN models, sufficient abundances of ^{56}Ni are produced in the silicon burning so that the early light curve is dominated by its total ejected mass, so the lower limit of the luminosity of the early SNR is a proportional function of the ^{56}Ni mass with a high tendency to similarity:

$$L(t) \gtrapprox \Theta(t)\Lambda(t)M_{\mathrm{Ni}} \tag{6.1}$$

While $\Theta(t)$, describing the energy release rate of ^{56}Ni per mass, is easily deducible[35] and not affected by ambient conditions, the transfer efficiency factor Λ is less trivial. As an estimate, the value determined from early light curve observations of SN2008ax (Type Ib) of $\Lambda = 0.95$ at the peak of the light curve was used in the analysis of Eriksen et al. (2009).
As described in Chapter 4.2, the interstellar extinction in the Milky Way is approximately inferable from the reddening and required to derive the luminosity from the observed magnitude. The common approach of determining the reddening by using the Balmer decrement is not applicable to Cas A because of the rarity of hydrogen throughout the remnant. There is little other choice than resort to lesser-researched metal transistions; the [FeII] 1.257 µm/1.644 µm line ratio is still subject of discussion with theoretical calculations varying over 30%, the most reliable source being results of the P-Cygni nebula observations which resulted in an empirical ratio of 1.49.
Spatially resolved observations, primarily conducted in the northwest of the remnant, show significant variation, resulting in A_V ranging from 5 to 13. This prohibits estimating a reasonably precise value for the center of the remnant devoid of iron emissions, where the SN can be presumed to have happened since there are no indicators of movement of the remnant in the POS. Eriksen et al. (2009) assume without further evidence that the infrared emissions of the CCO are dominated by synchrotron radiation to justify fitting these to a reddening coefficient and a power law (see Chapter 4.1), resulting in $A_V = 6.2 \pm 0.6$. The relative and absolute optical magnitudes m_V and M_V are correlated linearily as given by Equation 4.4 and repeated here for convenience:

$$m_v = M_V + A_V \tag{6.2}$$

To test the estimated extinction, SN1993J's peak $M_V = -17.5$ is adopted for Cas A, resulting in $m_V = -11.3$; while Type IIb SNe are in general inhomogeneous (SN1996cb for example exhibited a peak magnitude of -16.3), such an event would have definitely been noticed[36]. Eriksen et al. (2009) argue that, since Flamsteed's sighting occured in August and Krause et al. (2008) report a decline in magnitude of ~ 3 within 140 days for Cas A's LE, it is possible that the SN occured in winter, when Cas A transits the sky during daytime; while being still in a high position during the twilight, an initial $m_v \sim 3$, corresponding to $M_V \sim -3.2$, would have been visible, but not among the brightest objects on the sky, so that SN might have escaped initial attention.
In lack of better indicators, using the estimated extinction and unreasonably low brightness as argued above rewards with a remarkably unreliable upper ^{56}Ni ejecta mass limit of $0.16 M_\odot$. Considering that the extinction might very well have been variable in the previous 329 years makes this result even more questionable.
Despite best efforts, purely observational analysis fails to determine this important parameter,

[35] $\Theta(t) = \frac{N_a}{56}\left[\frac{E_{\mathrm{Ni}}}{\tau_{\mathrm{Ni}}}e^{-t/\tau_{\mathrm{Ni}}} + \frac{E_{\mathrm{Co}}}{\tau_{\mathrm{Co}}-\tau_{\mathrm{Ni}}}\left(e^{-t/\tau_{\mathrm{Co}}} - e^{-t/\tau_{\mathrm{Ni}}}\right)\right]$

[36] In comparison, a full moon averages at $m_V = -12.7$.

making it necessary to compare elaborate simulations to gather hints about Cas A's progenitor. In order to obtain a spatially resolved physical 2D model of a variety of parameters of Cas A, X-ray continuum emissions from 0.3 keV to 10 keV were fitted to a plasma model with temperature, ionisation state, electron density and elemental abundances as free parameters. As expected by Cas A's evolutionary phase transistion, a single plasma component model failed to produce a reasonable fit, so a cool and hot component were introduced with good results as exemplified in Figure 6.4 on the left.

Among other elemental abundances, this produced a total abundance of X-ray emitting iron of $0.058 M_\odot$ (Willingale et al. 2003). Being the isotope with the most efficient production path and making up 92% of all iron isotopes within our solar system, it is reasonable to assume that the bulk of the iron mass in Cas A is indeed ^{56}Fe. However, the geometry of Cas A suggests that there is a substantial non-luminescent iron inventory in the unshocked ejecta between the thick disks and probably in front of the large southeast piston, so while setting a hard lower limit for the mass of ^{56}Ni, an upper limit cannot be derived.

Furthermore, silicon, sulfur, calcium, argon, oxygen and nickel dominate derived mass distribution by far, ranging between $0.9 M_\odot$ (S) and $1.2 M_\odot$ (O). As the initial abundances of α nickel are virtually guaranteed to have decayed to minute traces, the X-ray emitting nickel is very likely to be a (quasi-)stable isotope. Interestingly, Si, S, Ca and Ar, being the four lightest elements in the α-ladder, are spatially tightly grouped and vary little in ratio over the entire SNR; there are no indicators of fusion neighbors to be more colocated than others.

Lastly, the simulation yielded estimates of the total visible plasma mass of $10 M_\odot$ of which 72% appear to be accreted CSM and a total energy of 1.03 B of which 32% are kinetic. This does not comply with the model shown in Figure 5.6: When assuming a kinetic explosion energy of 1 B, an ejecta mass of $1.4 M_\odot$ and a ratio of accreted CSM to plasma mass of 57% are predicted. Adjusting the CSM mass ratio of the simulation but leaving the total mass unchanged demands a kinetic explosion energy of 5.5 B; modifying this would stain the excellent correlation between the symmetric kinematic model and observations. However, in regard of the small solid angle covered by the pistons it is possible that considerably less energy is required to reach this state.

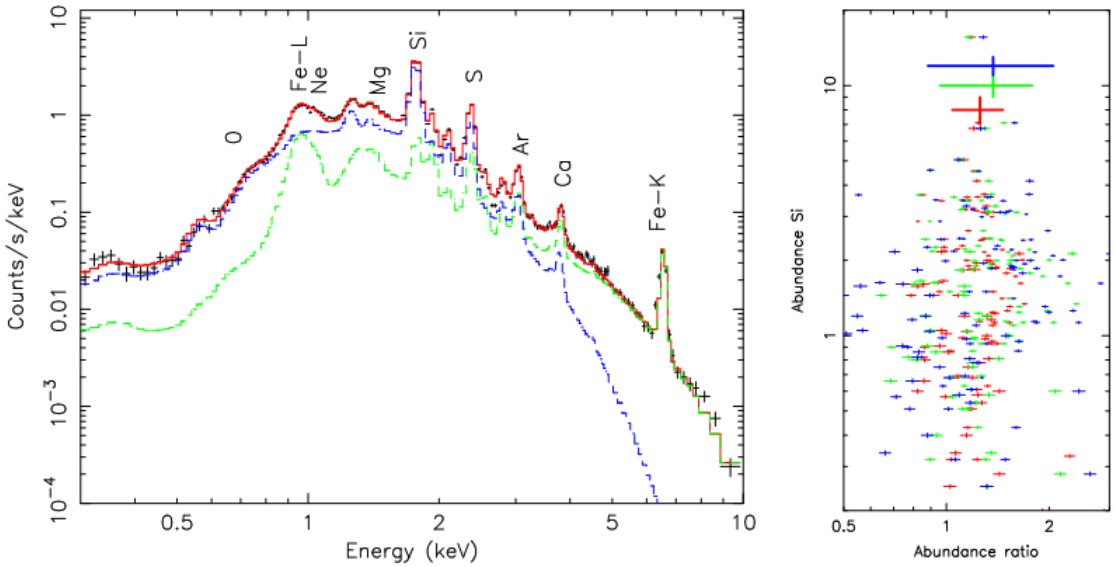

Figure 6.4: Plasma model fit of the X-ray continuum (Source: Bleeker et al. 2002). *Left:* Example of a X-ray spectrum of a $20'' \times 20''$ region of Cas A (black crosses) with a fitted two-component plasma (red) consisting of a cool component (blue) and a hot component (green). *Right:* Variance of abundance ratios of S/Si (red), Ar/Si (green) and Ca/Si (blue) at different POS locations (unmarked) on the remnant in contrast with the Si abundances at the respective positions. The large error bars on top indicate the mean and RMS scatter of the individual elements.

7 Discussion

Consistency of Geometry. With the piston and disk asymmetries in the shocked plateau, especially because of their symmetry plane being at a small angle to the POS, the initial derivation of the distance has to be reassessed. Given the good fit of the FMKs to a sphere as shown in 5.2, the most likely deceiving scenario would be an elliptical distribution of the FMKs. As the shock appears to unfold faster in the POS, an oblate FMK distribution might be likely, resulting in overestimating the distance. However, the primary symmetry plane of the shock is tilted by a significant angle to the POS, indicating that a major ellipticity would most likely be visible in the fit.
The derivations in the expansion speed of the recently shocked ejecta can be explained by their affiliation to large asymmetric structures, while the Doppler shifts in the optical domain suggest that the reverse shock is indeed approximately spherical. The forward shock however, being supported in the POS by the additional outflow of the pistons, might very well be oblate; the filaments that define its proportions have not yet been observed in the velocity space. The sphericity of the reverse shock may be compatible with an oblate shock front, assuming that the densities in-between adjust the speed of sound accordingly. This could be tested by analysing the large-scale gradient movement through the doppler shift nearby the remnant's center in the POS; while on the back of the remnant, the thin disk might overshadow this, the distinctly three-dimensional interwoven filament structure in the front might allow such a investigation.
While the validity of the doppler mapping in the shocked plateau is not properly backed, but rather questioned by the author's theory of diversion from the straight path from the COE of ejecta nearby the structural transistions, its results are consistent and demonstrate that the formerly assumed layer overturn has not happened and thereby valuable even without certainity about distortions in the 3D projection.

Progenitor. The SN type has been determined with little doubt to be the rare IIb subclass. Little empirical knowledge exists to tie remnant's evolution to the origins; however, the anomalously huge abundance of the rarely observed ^{44}Ti suggests that there was a particularily intense α-rich freeze-out. Considering that the now-observed asymmetries imply the possibility of strong turbulences early after the SN, the spatial proximity of low-order α-elements and apparent similar distribution throughout the remnant suggests that the freeze-out was long-lived.
The dense rings in the unshocked ejecta appear to enclose cavities. It is noteworthy that they do not align particularily well with the pistons; large cavities in the northeast and south are located in-between the pistons. Based on the concept by Milisavljevic and Fesen (2015) that these were created by radioactive clusters and the titanium maps in Grefenstette et al. (2014) that show a cluster in the northern cavity, the author suspects that these might have been regions of intense and long lasting freeze-out.
This is further supported by the hypothesis that Type IIb SNe might emerge from binaries of which the larger star consists predominately of helium. In comparison to SN1993J, the P-Cygni line found in Cas A's light echo is less pronounced, indicating that the ejected helium shell might have been of lesser mass; whether this is due to a higher helium ratio mixing in the slow ejecta or a smaller initial abundance in the first place is debateable.

Subluminosity of the Supernova. The absence of reports about Cas A's explosion is usually allocated to an assumed subluminosity. The measurements of the extinction towards Cas A did not provide a consistent answer, even though small areas of sufficient extinction have been detected, suggesting the possibility of a dense cloud absorbing the explosion's early light curve. The structure in the shocked plateau however reveals that there is an apparent spatial inhomogenity in the energy output of Cas A, and the observation of light echoes indicate that this property has emerged shortly after the SN. The apparent axis of minimum (kinetic) energy

output is aligned close to the LOS; however, as the early lightcurve is dominated by radioactive heating of the debris and distribution of the kinetic energy on POS expansion rather than LOS expansion can be expected to result in the opposite. An intially inverted behavior and subsequent kickback is not impossible, but there are no indicators observed to support this and no similar behavior known from other SNe.
Another option might be that Cas A was extremely rich in helium after the explosion and large amounts of ^{56}Ni were reabsorbed into the α-ladder, reducing its radiative heating. Whether such a process might however decrease the energy output by the required magnitude is highly questionable.

Acknowledgments. The author thanks Roland Diehl for providing an expansive topic to get introduced in stellar astronomy, guidance through the orientation process and for fostering a work climate characterized by frequent exchange of knowledge and experience, Thomas Siegert for his willingness to discuss a variety of naive notions as well as dedicating time and effort to reviewing parts of this thesis, Domenico Gallipoli and Joao Mendes for an introduction to the scientific process and academic writing and Ferdinand Euchter and Antje Urswurff for lessons in professionalism.

References

P. J. Armitage. Dynamics of Protoplanetary Disks. ARA&A, 49:195–236, Sept. 2011. doi: 10.1146/annurev-astro-081710-102521.

G. Bellini, J. Benziger, D. Bick, S. Bonetti, G. Bonfini, D. Bravo, M. Buizza Avanzini, et al. First Evidence of pep Solar Neutrinos by Direct Detection in Borexino. *Physical Review Letters*, 108(5):051302, Feb. 2012. doi: 10.1103/PhysRevLett.108.051302.

L. Bildsten, K. J. Shen, N. N. Weinberg, and G. Nelemans. Faint Thermonuclear Supernovae from AM Canum Venaticorum Binaries. ApJ, 662:L95–L98, June 2007. doi: 10.1086/519489.

J. Bleeker, J. Vink, K. van der Heyden, D. Willingale, J. Kaastra, and M. Laming. A synoptic spectral study of Cassiopeia-A based on XMM-Newton and BeppoSax observations. *ArXiv Astrophysics e-prints*, Feb. 2002.

D. Branch, M. Livio, L. R. Yungelson, F. R. Boffi, and E. Baron. In Search of the Progenitors of Type IA Supernovae. PASP, 107:1019, Nov. 1995. doi: 10.1086/133657.

G. E. Brown and H. A. Bethe. A Scenario for a Large Number of Low-Mass Black Holes in the Galaxy. ApJ, 423:659, Mar. 1994. doi: 10.1086/173844.

T. DeLaney and L. Rudnick. The First Measurement of Cassiopeia A's Forward Shock Expansion Rate. ApJ, 589:818–826, June 2003. doi: 10.1086/374813.

T. DeLaney, L. Rudnick, M. D. Stage, J. D. Smith, K. Isensee, J. Rho, G. E. Allen, H. Gomez, T. Kozasa, W. T. Reach, J. E. Davis, and J. C. Houck. The Three-dimensional Structure of Cassiopeia A. ApJ, 725:2038–2058, Dec. 2010. doi: 10.1088/0004-637X/725/2/2038.

O. Demircan and G. Kahraman. Stellar mass-luminosity and mass-radius relations. Ap&SS, 181:313–322, July 1991. doi: 10.1007/BF00639097.

R. L. Dickman. The ratio of carbon monoxide to molecular hydrogen in interstellar dark clouds. ApJS, 37:407–427, Aug. 1978. doi: 10.1086/190535.

R. Diehl and F. X. Timmes. Gamma-Ray Line Emission from Radioactive Isotopes in Stars and Galaxies. PASP, 110:637–659, June 1998. doi: 10.1086/316169.

M. M. Dunham, X. Chen, H. G. Arce, T. L. Bourke, S. Schnee, and M. L. Enoch. Detection of a bipolar molecular outflow driven by a candidate first hydrostatic core. *The Astrophysical Journal*, 742(1):1, 2011. URL `http://stacks.iop.org/0004-637X/742/i=1/a=1`.

Z. Eker, F. Soydugan, E. Soydugan, S. Bilir, E. Yaz Gökçe, I. Steer, M. Tüysüz, T. Şenyüz, and O. Demircan. Main-Sequence Effective Temperatures from a Revised Mass-Luminosity Relation Based on Accurate Properties. AJ, 149:131, Apr. 2015. doi: 10.1088/0004-6256/149/4/131.

K. A. Eriksen, D. Arnett, D. W. McCarthy, and P. Young. The Reddening Toward Cassiopeia A's Supernova: Constraining the ^{56}Ni Yield. ApJ, 697:29–36, May 2009. doi: 10.1088/0004-637X/697/1/29.

R. A. Fesen, M. C. Hammell, J. Morse, R. A. Chevalier, K. J. Borkowski, M. A. Dopita, C. L. Gerardy, S. S. Lawrence, J. C. Raymond, and S. van den Bergh. The Expansion Asymmetry and Age of the Cassiopeia A Supernova Remnant. ApJ, 645:283–292, July 2006a. doi: 10.1086/504254.

R. A. Fesen, G. G. Pavlov, and D. Sanwal. Near-Infrared and Optical Limits for the Central X-Ray Point Source in the Cassiopeia A Supernova Remnant. ApJ, 636:848–858, Jan. 2006b. doi: 10.1086/498087.

E. V. Gotthelf, B. Koralesky, L. Rudnick, T. W. Jones, U. Hwang, and R. Petre. Chandra Detection of the Forward and Reverse Shocks in Cassiopeia A. ApJ, 552:L39–L43, May 2001. doi: 10.1086/320250.

R. J. Gould and E. E. Salpeter. The Interstellar Abundance of the Hydrogen Molecule. I. Basic Processes. ApJ, 138:393, Aug. 1963. doi: 10.1086/147654.

B. W. Grefenstette, F. A. Harrison, S. E. Boggs, S. P. Reynolds, C. L. Fryer, K. K. Madsen, D. R. Wik, A. Zoglauer, C. I. Ellinger, D. M. Alexander, H. An, D. Barret, F. E. Christensen, et al. Asymmetries in core-collapse supernovae from maps of radioactive ^{44}Ti in CassiopeiaA. Nature, 506:339–342, Feb. 2014. doi: 10.1038/nature12997.

S. F. Gull. A numerical model of the structure and evolution of young supernovaremnants. MNRAS, 161:47–69, 1973. doi: 10.1093/mnras/161.1.47.

D. Guszejnov and P. F. Hopkins. Star formation in a turbulent framework: from giant molecular clouds to protostars. MNRAS, 459:9–20, June 2016. doi: 10.1093/mnras/stw619.

A. Heger, C. L. Fryer, S. E. Woosley, N. Langer, and D. H. Hartmann. How Massive Single Stars End Their Life. ApJ, 591:288–300, July 2003. doi: 10.1086/375341.

K. Isensee, L. Rudnick, T. DeLaney, J. D. Smith, J. Rho, W. T. Reach, T. Kozasa, and H. Gomez. The Three-dimensional Structure of Interior Ejecta in Cassiopeia A at High Spectral Resolution. ApJ, 725:2059–2070, Dec. 2010. doi: 10.1088/0004-637X/725/2/2059.

G. H. Jacoby, D. Branch, R. Ciardullo, R. L. Davies, W. E. Harris, M. J. Pierce, C. J. Pritchet, J. L. Tonry, and D. L. Welch. A critical review of selected techniques for measuring extragalactic distances. PASP, 104:599–662, Aug. 1992. doi: 10.1086/133035.

S. Jha, A. G. Riess, and R. P. Kirshner. Improved distances to type ia supernovae with multicolor light-curve shapes: Mlcs2k2. *The Astrophysical Journal*, 659(1):122, 2007. URL `http://stacks.iop.org/0004-637X/659/i=1/a=122`.

Y. Kamiya, M. Tanaka, K. Nomoto, S. I. Blinnikov, E. I. Sorokina, and T. Suzuki. Super-Chandrasekhar-mass Light Curve Models for the Highly Luminous Type Ia Supernova 2009dc. ApJ, 756:191, Sept. 2012. doi: 10.1088/0004-637X/756/2/191.

T. Khanzadyan, M. D. Smith, R. Gredel, T. Stanke, and C. J. Davis. Active star formation in the large Bok globule CB 34. A&A, 383:502–518, Feb. 2002. doi: 10.1051/0004-6361:20011531.

B. Koralesky, L. Rudnick, E. V. Gotthelf, and J. W. Keohane. The X-Ray Expansion of the Supernova Remnant Cassiopeia A. ApJ, 505:L27–L30, Sept. 1998. doi: 10.1086/311604.

O. Krause, S. M. Birkmann, T. Usuda, T. Hattori, M. Goto, G. H. Rieke, and K. A. Misselt. The Cassiopeia A Supernova Was of Type IIb. *Science*, 320: 1195, May 2008. doi: 10.1126/science.1155788.

R. B. Larson. Numerical calculations of the dynamics of collapsing proto-star. MNRAS, 145:271, 1969. doi: 10.1093/mnras/145.3.271.

A. Maeder and G. Meynet. Tables of evolutionary star models from 0.85 to 120 solar masses with overshooting and mass loss. A&AS, 76:411–425, Dec. 1988.

C. F. McKee and E. C. Ostriker. Theory of Star Formation. ARA&A, 45:565–687, Sept. 2007. doi: 10.1146/annurev.astro.45.051806.110602.

D. Milisavljevic and R. A. Fesen. The bubble-like interior of the core-collapse supernova remnant Cassiopeia A. *Science*, 347:526–530, Jan. 2015. doi: 10.1126/science.1261949.

Minkowski. Paris Symposium on Radio Astronomy. In R. Bracewell, editor, *Paris Symposium on Radio Astronomy*, pages 315–322. Stanford University Press, 1959.

G. G. Pavlov and G. J. M. Luna. A Dedicated Chandra ACIS Observation of the Central Compact Object in the Cassiopeia A Supernova Remnant. ApJ, 703:910–921, Sept. 2009. doi: 10.1088/0004-637X/703/1/910.

M. M. Phillips. The absolute magnitudes of Type IA supernovae. ApJ, 413:L105–L108, Aug. 1993. doi: 10.1086/186970.

J. E. Reed, J. J. Hester, A. C. Fabian, and P. F. Winkler. The Three-dimensional Structure of the Cassiopeia A Supernova Remnant. I. The Spherical Shell. ApJ, 440:706, Feb. 1995. doi: 10.1086/175308.

A. Rest, R. J. Foley, B. Sinnott, D. L. Welch, C. Badenes, A. V. Filippenko, M. Bergmann, W. A. Bhatti, S. Blondin, P. Challis, G. Damke, H. Finley, M. E. Huber, D. Kasen, et al. Direct Confirmation of the Asymmetry of the Cas A Supernova with Light Echoes. ApJ, 732:3, May 2011. doi: 10.1088/0004-637X/732/1/3.

T. Siegert, R. Diehl, M. G. H. Krause, and J. Greiner. Revisiting INTEGRAL/SPI observations of ^{44}Ti from Cassiopeia A. A&A, 579:A124, July 2015. doi: 10.1051/0004-6361/201525877.

J. D. T. Smith, L. Rudnick, T. Delaney, J. Rho, H. Gomez, T. Kozasa, W. Reach, and K. Isensee. Spitzer Spectral Mapping of Supernova Remnant Cassiopeia a. ApJ, 693:713–721, Mar. 2009. doi: 10.1088/0004-637X/693/1/713.

K. Takahashi, T. Yoshida, and H. Umeda. Evolution of Progenitors for Electron Capture Supernovae. ApJ, 771:28, July 2013. doi: 10.1088/0004-637X/771/1/28.

J. R. Thorstensen, R. A. Fesen, and S. van den Bergh. The Expansion Center and Dynamical Age of the Galactic Supernova Remnant Cassiopeia A. AJ, 122: 297–307, July 2001. doi: 10.1086/321138.

J. K. Truelove and C. F. McKee. Evolution of Nonradiative Supernova Remnants. ApJS, 120:299–326, Feb. 1999. doi: 10.1086/313176.

R. Willingale, J. A. M. Bleeker, K. J. van der Heyden, J. S. Kaastra, and J. Vink. X-ray spectral imaging and Doppler mapping of Cassiopeia A. A&A, 381:1039–1048, Jan. 2002. doi: 10.1051/0004-6361:20011614.

R. Willingale, J. A. M. Bleeker, K. J. van der Heyden, and J. S. Kaastra. The mass and energy budget of Cassiopeia A. A&A, 398:1021–1028, Feb. 2003. doi: 10.1051/0004-6361:20021554.

L. Woltjer. Supernova Remnants. ARA&A, 10:129, 1972. doi: 10.1146/annurev.aa.10.090172.001021.

S. Woosley and T. Janka. The physics of core-collapse supernovae. *Nature Physics*, 1:147–154, Dec. 2005. doi: 10.1038/nphys172.

Appendices

A.1 Small Angle Approximation on the POS

When observing two objects in the same distance D under an angle θ, the distance between x them is given by $x = 2D\sin(\frac{\theta}{2})$. When approximating this with $x \approx x^* = D\theta$, the relative error is:

$$\delta_{\text{rel}}(x) = \left|\frac{x^*}{x} - 1\right| = \frac{\theta}{2\sin\frac{\theta}{2}} - 1 \tag{.1}$$

So with a total covered angle angle of $\theta^{\max} = 4'$, the maximum deviation is $\delta_{\text{rel}}^{\max}(x) = 6 \times 10^{-8}$.

A.2 Drag on FMKs

Given a multitude of objects with the observed angular distance θ_n and Doppler velocity $\dot{z}_n$, both relative to the COE, and using the small angle approximation from above, the distance traveled in the POS is $x = D\theta$ and the distance traveled LOS during the time since the explosion is $z = \dot{z}\Delta T$. A perfectly spherical structure with actual radius R resp. observed angular radius ρ demands:

$$\exists R : \forall n : R^2 = D^2\theta_n^2 + \Delta T^2 \dot{z}_n^2 \quad \text{or} \quad \exists \rho : \forall n : \dot{z}_n^2 = \left(\rho^2 - \theta_n^2\right)\left(\frac{D}{\Delta T}\right)_{\text{lin}}^2 \tag{.2}$$

Assuming laminar drag in a homogeneous[37] medium, so that $\ddot{r} = -c\dot{r}$ with arbitrary drag constant c, the position on the LOS is related to the observed velocity by the following formula:

$$z = \frac{\dot{z}}{c}\left(e^{ct} - 1\right) \approx \dot{z}t\left(1 + \frac{ct}{2}\right) \tag{.3}$$

Modifying Equation .2 accordingly results in:

$$\left(\frac{D}{\Delta T}\right)_{\text{drag}} \approx \left(1 + \frac{c\Delta T}{2}\right)\left(\frac{D}{\Delta T}\right)_{\text{lin}} \tag{.4}$$

Thereby, subsequent measurements of preferably the same set of FMKs should show a decline in $(D/\Delta T)_{\text{lin}}$. When disregarding the error bar of the age result in Chapter 5.1 and allocating the discrepancy from Flamsteeds observation (this time interval being T_f) to the assumed simple drag model in order to estimate its repercussions on the measurement of $D/\Delta T$, the drag constant is given by:

$$Tc = e^{cT_f} - 1 \quad \xrightarrow{\text{Taylor approx.}} \quad c \approx -\frac{3}{2T_f} + \sqrt{\frac{6}{T_f^3}\left(T - \frac{5}{8}T_f\right)} \tag{.5}$$

Having velocity information from 2004, $T = 332$ a and $T_f = 324$ a so that $c = 1.5 \times 10^{-4}$ a^{-1}. According to Equation .4, this results in an inaccuracy of $\delta_{\text{rel}} D/\Delta T = 0.024$ and $\delta_{\text{abs}} D = 85$ pc, so it is in the same magnitude as the inaccuracy of the fit.

[37] While this assumption is questionable, the order of magnitude of the results should be mostly unaffected by choosing a reasonable CSM viscosity gradient.